

# The Power of Genetic Algorithms: what remains of the pMSSM?

Steven Abel,<sup>1,\*</sup> David G. Cerdeño,<sup>1,†</sup> and Sandra Robles<sup>2,‡</sup>

<sup>1</sup>*Institute for Particle Physics Phenomenology,  
Durham University, Durham DH1 3LE, United Kingdom*

<sup>2</sup>*ARC Centre of Excellence for Particle Physics at the Terascale,  
School of Physics, The University of Melbourne, Victoria 3010, Australia*

Genetic Algorithms (GAs) are explored as a tool for probing new physics with high dimensionality. We study the 19-dimensional pMSSM, including experimental constraints from all sources and assessing the consistency of potential signals of new physics. We show that GAs excel at making a fast and accurate diagnosis of the cross-compatibility of a set of experimental constraints in such high dimensional models. In the case of the pMSSM, it is found that only  $\mathcal{O}(10^4)$  model evaluations are required to obtain a best fit point in agreement with much more costly MCMC scans. This efficiency allows higher dimensional models to be falsified, and patterns in the spectrum identified, orders of magnitude more quickly. As examples of falsification, we consider the muon anomalous magnetic moment, and the Galactic Centre gamma-ray excess observed by Fermi-LAT, which could in principle be explained in terms of neutralino dark matter. We show that both observables cannot be explained within the pMSSM, and that they provide the leading contribution to the total goodness of the fit, with  $\chi^2_{\delta a_\mu^{\text{SUSY}}} \approx 12$  and  $\chi^2_{\text{GCE}} \approx 155$ , respectively.

---

\* s.a.abel@durham.ac.uk

† d.g.cerdeno@durham.ac.uk

‡ sandra.robles@unimelb.edu.au

## I. INTRODUCTION

Experimental constraints on supersymmetry continue to make the simplest realisations of the Minimal Supersymmetric Standard Model (MSSM) less credible. One is forced to consider less constrained alternatives such as the pMSSM [1]. This is the most general version of the  $R$ -parity conserving MSSM under the assumption of CP conservation, Minimal Flavour Violation, and degenerate first and second generation sfermion masses<sup>1</sup>. It has a multi-dimensional parameter space – 23 in total, consisting of 19 fundamental parameters and 4 nuisance parameters.

Analysis of such high dimensionality models becomes very difficult. The traditional technique of “slice-and-scan” that suffices for the Constrained MSSM (CMSSM) for example, is entirely infeasible. Typically one uses Monte-Carlo and nested sampling approaches as in Refs. [2–5]. It is probably fair to say that, even if analysis can be made feasible by these methods, it is not always clear what one should conclude from the results. Suppose for instance that upon scanning a 23D cube of the parameter space of the pMSSM one found that in every 2 dimensional slice the allowed region occupies the inside of a circle that just touches the edges of the cube. This “allowed ball” would appear to almost fill the 23D cube inside which it just fits, and yet it would actually occupy only 0.4% of the volume. This is the infamous “large dimensionality problem”: taking slices of a high dimensional object inevitably gives a very misleading impression of its structure. On a more practical level, how can one attempt to falsify a model such as the pMSSM, when superficially it seems that virtually any set of observables could be accommodated somewhere in the parameter-space? And compounding the problem associated with the multi-modality of variables, is the multi-modality of observables. If several suitable areas of parameter space are discovered, do they represent a single cluster or several disjoint favoured regions? Do they give a prediction for the spectrum? Which observables have most influence over the favoured regions?

All of these issues suggest the use of heuristic search and visualisation techniques. In this paper we consider the effectiveness of Genetic Algorithms (GAs), in assessing and analysing the pMSSM. GAs seek optimal solutions by evolving a population of models in the search-space which, by means of a suitable definition of “fitness”, is transformed into a fitness landscape [6–11]. In the case of models such as the pMSSM the optimisation in question is of course to find the minimum overall  $\chi^2$ , whose inverse can therefore serve directly as a measure of the fitness. There are several advantages of GAs that this study will highlight. The first is simply the extreme efficiency of such techniques versus traditional scanning techniques, or even more sophisticated Bayesian Inference techniques, such as that employed by MultiNest [12–14]. Indeed, compared to the latter, GAs can find a best fit point orders of magnitude more quickly, because the number of models that need to be built is considerably smaller<sup>2</sup>. As a practical demonstration, we show that with this approach it is easily possible to exclude the pMSSM, and to identify the main culprit that apparently cannot be reconciled with experiment in any of the parameter space, namely  $(g-2)_\mu$ . It becomes clear that a GA can efficiently find regions of parameter space in which the  $\chi^2$  of all other parameters are reasonable, with  $(g-2)_\mu$  standing out as the dominant contribution. In the present case only  $\sim 10^4$  models need to be evaluated in order to reach this conclusion<sup>3</sup>. While they are not exhaustive in the usual sense, GAs *do* probe the entire search-space, albeit in a highly non-linear way [6]. Therefore, one can now be confident that the pMSSM does not have any remaining regions of parameter space that harbour better solutions for  $(g-2)_\mu$ . However, no other observable is particularly problematic to fit.

Another advantage of GAs arises from the fact that they are a dynamical process. It has been argued that whether a problem is “GA-hard” or “GA-easy” depends on the “fitness-distance correlation” in the parameter space [15, 16]. Problems that are GA-hard (or that are not tackled well) resemble “needle-in-a-haystack” problems, in which all incorrect solutions are equally bad and one has as much chance of landing on the correct solution as when performing a random scan. In this context, it is important that the GA is performed so that a “fitness landscape” is established as a function of continuous parameters such as  $\chi^2$ . Any hard experimental exclusions are essentially step-functions

<sup>1</sup> Usually the pMSSM is defined with these last two conditions imposed at the electroweak scale, but for this study it will make little difference if we impose them at the Grand Unified Theory (GUT) scale.

<sup>2</sup> We should remark that we checked the consistency of our procedure using MultiNest in the CMSSM.

<sup>3</sup> For comparison, it is worth point out that performing a flat scan even as rudimentary as taking one large and one small value for each parameter would require  $10^7$  evaluations.

in the fitness landscape that can locally weaken the fitness-distance correlation. This fitness-distance correlation is made manifest by the flow of the population as it evolves in the GA. By observing this flow over successive generations, one sees the pull of various observables. Naturally those that are well constrained experimentally within the parameter space, for example soft-terms such as  $A_t$  that govern the Higgs mass, exert a strong pull (through the contribution to  $\chi^2$ ), and the population evolves rapidly towards suitable values. Conversely, the limited precision in the measured Higgs couplings leads to less focused values for e.g.  $\tan\beta$ . In the SUSY context, this can be thought of as a measure of the fine-tuning in the theory. Such flows *can* incidentally be understood by taking slices of the space of observables, where it becomes clear if a particular observable is becoming significantly focussed. The efficiency of GAs in this context compared to other techniques suggests that the problem of optimising  $\chi^2$  for a multi-modal model such as the pMSSM is very “GA-easy”: the fitness-distance correlation (by virtue of  $\chi^2$ ) is very good.

A final advantage of GAs lies in their end product, which (by construction) is a large population of models focussed around those regions of parameter space that are the most interesting given the current constraints. This provides a natural tool with which new observables can be tested. The example we will consider here is the Fermi-LAT Galactic Centre excess. Given such a new observable, one could of course just fold it into the original study and start from the beginning. But one can also, either test the final population to see if it predicts the observed value, or even better add the new observable into the fitness of the final population and continue to evolve it to a new equilibrium. If the new best fit is considerably worse than the old one, then we can conclude that the new observable is in conflict with the model. This is a natural approach to take when new experimental results need to be taken into consideration. In this sense GAs are able to provide a (literally) evolving population of “Snowmass points”.

The paper is organized as follows. In Section II we briefly review the GA technique, and in Section III we explain how we apply it to the specific case of the pMSSM, with 19 parameters defined at the GUT scale and 4 nuisance parameters. We also discuss there the different experimental constraints that are included in our analysis. The results are presented in Section IV, analysing first the case of the muon anomalous magnetic moment and then the Galactic Centre gamma-ray excess. The conclusions are presented in Section V. Finally, Appendix A contains some complementary plots that illustrate the evolution of the GA in the pMSSM parameter space.

We should mention where this work stands in relation to previous studies. In fact in our view the number of studies in the High Energy Physics arena employing GAs is still remarkably small considering the robustness and utility of the technique. It has been used in the model building context in Refs. [17, 18]. In those cases the construction of fitness landscape is more directly related to desirable properties such as small positive cosmological constant, number of generations and so-forth. As such one is looking for a small number of “perfect solutions”, and the technique becomes more of a “black-art”. In the model-exclusion/profile-likelihood context it was discussed in Refs. [19–21]. The main body of the study conducted here is most closely related to Ref. [21]<sup>4</sup>, but in a much higher dimensionality.

## II. THE GENETIC ALGORITHM TECHNIQUE

We begin by briefly reviewing the GA technique with specific reference to the task at hand (for more pedagogical introductions see Refs. [9, 18, 20]), namely surveying regions of model parameter space, excluding disfavoured regions and selecting favoured regions of some framework. The physical “observable” we wish to optimise in the parameter-space is the overall  $\chi^2$ . We shall focus in particular on the particular properties of the PIKAIA 1.2 package which is used here to perform the GA [22–25].

Any GA is an optimisation based on evolving a population of  $N_{\text{pop}}$  trial individuals, typically 50-100. Each individual consists of a string of data (the so-called *chromosome*), that encodes the parameters defining a particular individual. This encoding can take various forms, and is referred to generically as the individual’s *genotype*. In this case, it is simply all the input parameters collected

---

<sup>4</sup> Our GA implementation is based on the publicly available PIKAIA code, first introduced in Refs. [22, 23].

together in one long string of data. The entries in the chromosome are called *alleles*. Often a binary encoding is preferred as it can work with smaller populations, however PIKAIA 1.2 uses a decimal encoding. It is convenient to also introduce the notion of uniformly sized small groups of alleles, called *genes*, that each encode a single physical parameter, for example a soft-mass squared. The population is initially chosen with random genomes for the  $N_{\text{pop}}$ -individuals, and then the algorithm consists of repeated application of the following three basic elements:

**Selection:** Individuals are first selected from the population to make “breeding pairs”. If the population size is preserved (the usual scheme) then there will be  $N_{\text{pop}}$  breeding pairs, and the average individual will be selected for breeding twice. The first step in this process is to assign to each individual a *fitness* based on its physical properties (the *phenotype*). In the present case, the phenotype is the collection of all the experimental observables of interest, for example Higgs masses, decay widths, and so forth. The fitness is a single function of all these variables whose theoretical maximum value corresponds to the perfect individual. In this study, the fitness function is taken to be  $1/\chi^2$  (typically the convergence to solutions is quite independent of this function). This step is usually the most case-dependent and time-intensive part of the whole procedure, because it is where the physics is bolted on.

Once fitnesses have been assigned to the entire population, breeding pairs are formed by selecting individuals based on their fitness (with obviously fitter individuals being selected more often). Typically the fittest individual may breed a few times more than the average, but it is important that less fit individuals are allowed to mate. The selection process may take many different forms, such as roulette-wheel, rank-weighting, tournament selection, and so on<sup>5</sup>.

**Breeding/Cross-over:** A new population of individuals is formed by splicing together the chromosomes of the two individuals in each breeding pair. Again there are many different ways to do this, but a typical choice (uniform cross-over) might be to cut the chromosomes at two random points along their length and swap the middle sections. PIKAIA 1.2 uses both one- and two-point cross-over in roughly equal proportions to reduce end-point biasing.

**Mutation:** With only the two previous elements, one would already observe convergence of the population around good solutions over generations. However, the real power of GAs comes from the third element which is *mutation*. This is the feature which is chiefly responsible for the orders-of-magnitude gain in efficiency over a simple Monte-Carlo. Once a new generation is formed, a small fraction (usually around a percent) of the alleles have their values flipped at random. This prevents stagnation in the population, where the entire population clusters around a local maximum in the fitness, when there are better solutions globally. It is important to understand that mutation is not just an improvement to the convergence, but is absolutely integral to the entire process. Depending on the problem and the structure of the fitness landscape, the net effect is a dramatic increase in the overall rate of convergence. (As can be seen practically by optimising the mutation rate.) One of the innovations of PIKAIA 1.2 in this aspect is its use of *creep mutation* in order to overcome the so-called Hamming walls, which occur when the population is close to an optimum solution in terms of phenotype, but far away in terms of Hamming distance: for example the number 0.999 versus 1.000 requires a change in all 4 digits, but this very large change in genotype produces a very small change in phenotype. In short, creep-mutation “carries the 1” if a “9” is mutated by adding +1. As this kind of mutation results in small moves in physical parameter space, PIKAIA 1.2 invokes creep-mutation and one-point mutation with equal probability. This modification is also expected to mitigate somewhat the drawbacks of using decimal instead of binary encoding.

And then the process repeats. We should add that, so that the maximum fitness is monotonically increasing, it is common at this point to copy the fittest individual from the last generation into the new one and to kill the least fit new individual, known as *elitist selection*. The particular parameters

---

<sup>5</sup> Note that one does not always have to take the fitness to be a continuous function of the phenotype. For example, for problems where this would give a very wide and shallow fitness plateau, it is preferable to base the fitness of individuals on their ranking. This reproduces some of the advantages of tournament selection but is much simpler to incorporate.

used for this study are shown in Table I.

In summary, a GA incorporates and balances competing forces. Selection and breeding tends to produce convergence around local maxima in the fitness landscape, drawing the population in over generations. On the other hand the effect of mutation is to push the population away from local maxima (on average), so that as a whole it can explore the entire parameter space. The power of GAs then is in their ability to keep performing, regardless of the dimensionality of the physical parameter-space, which can even as large as the chromosome itself (as was the case of Ref. [18]), and in their ability to be sensitive to the entire landscape, but simultaneously respond to and converge on interesting regions. Note that there are many other practical elements, such as fitness “crowding penalties”, and “niching”, that we do not discuss (or use). They are covered in the literature (see Refs. [9, 10]) along with the underlying reasons for the effectiveness of GAs, such the Schema theorem.

Parameter	Value
Population, $N_{\text{pop}}$	100
Generations, $N_{\text{gen}}$	300
Length of gene	5
Crossover probability	0.85
Mutation mode	2 (adjustable rate based on fitness)
Initial mutation rate	0.005
Min. mutation rate	0.0005
Max. mutation rate	0.25
Relative fitness differential	1.0 (breeding probability equals to rank)
Reproduction plan	1 (full generational replacement)
Elitism	1 (keep best)

TABLE I. PIKAIA 1.2 control parameters used in this study.

### III. APPLICATION TO THE PMSSM

We now turn to the object of study, which is the phenomenological MSSM (pMSSM), with its 19 fundamental parameters. Here we define them at the Grand Unification Theory (GUT) scale and take  $\text{sign}(\mu) = 1$ . (In its usual definition the pMSSM takes parameters at the weak scale, however as a GA is not frequentist there is essentially no difference except for the effect of running on flavour degeneracy and consequently flavour changing observables. These effects are expected to be negligible for this study given that experimental constraints ultimately favour very large soft-terms. Note that  $\delta a_\mu$  will be important, but precise first/second generation degeneracy would have little bearing on it.) As well as these parameters, we include four additional parameters to account for the SM parameters with the largest uncertainties that could have an impact on the final theoretical predictions. These nuisance parameters are: the electromagnetic coupling constant evaluated at the Z-boson pole mass,  $\alpha_{\text{EM}}(M_Z)^{\overline{MS}}$ , the strong coupling constant at  $M_Z$ ,  $\alpha_S(M_Z)^{\overline{MS}}$ , the pole mass of the top quark,  $m_t$  and the pole mass of the bottom quark,  $m_b$ <sup>6</sup>. Their central values and uncertainties are given in Table II. Hence, there is a 23 dimensional parameter space, whose range of variation is listed in Table III. We restrict the study to positive gaugino masses, due to convergence issues in the selected SUSY spectrum calculator which occurred when negative gaugino masses were present<sup>7</sup>.

In order to evaluate the fitness as a function of the initial parameters, the pMSSM predictions were implemented in a joint likelihood comprising the following experimental constraints:

<sup>6</sup> For simplicity, we use the pole mass of the bottom quark as an input parameter instead of  $m_b(m_b)^{\overline{MS}}$ , since the bottom pole mass is an input of ZFITTER, the package used to compute the SM contributions to the Z boson decay width (see text below). In fact,  $m_b(m_b)^{\overline{MS}}$  and  $m_c(m_c)^{\overline{MS}}$  are calculated by ZFITTER, therefore for consistency we used these running masses as input parameters of the other packages mentioned throughout this work.

<sup>7</sup> Note that this analysis can be easily extended to regions of the parameter space with a negative  $\mu$  parameter and negative values of the soft masses.

Observable	Value
$\left[\alpha_{\text{EM}}(M_Z)^{\overline{MS}}\right]^{-1}$	$127.950 \pm 0.017$
$\alpha_S(M_Z)^{\overline{MS}}$	$0.1185 \pm 0.0006$
$m_b(\text{GeV})$	$4.78 \pm 0.06$
$m_t(\text{GeV})$	$173.1 \pm 0.6$

TABLE II. Standard model nuisance parameters, central values and uncertainties [26].

Parameter	Range
SM	
$\left[\alpha_{\text{EM}}(M_Z)^{\overline{MS}}\right]^{-1}$	[127.882, 128.018]
$\alpha_S(M_Z)^{\overline{MS}}$	[0.1161, 0.1209]
$m_b(\text{GeV})$	[4.54, 5.02]
$m_t(\text{GeV})$	[170.1, 175.5]
pMSSM (GUT scale)	
$M_1, M_2, M_3(\text{GeV})$	[50, 10000]
$m_{H_u}, m_{H_d}(\text{GeV})$	[50, 10000]
$m_{\tilde{Q}_{1,2}}, m_{\tilde{Q}_3}(\text{GeV})$	[50, 10000]
$m_{\tilde{U}_{1,2}}, m_{\tilde{U}_3}(\text{GeV})$	[50, 10000]
$m_{\tilde{D}_{1,2}}, m_{\tilde{D}_3}(\text{GeV})$	[50, 10000]
$m_{\tilde{L}_{1,2}}, m_{\tilde{L}_3}(\text{GeV})$	[50, 10000]
$m_{\tilde{E}_{1,2}}, m_{\tilde{E}_3}(\text{GeV})$	[50, 10000]
$A_t, A_b, A_\tau(\text{TeV})$	[-10, 10]
$\tan \beta$	[2, 62]

TABLE III. SM nuisance parameters and pMSSM input parameters defined at the GUT scale.

- **Electroweak precision observables (EWPOs):** i.e.  $Z$  pole observables and  $M_W$ . The theoretical prediction for the  $W$  boson pole mass  $M_W$  were calculated with **SOFTSUSY** 4.1.0 [27], and the effective electroweak mixing angle for leptons  $\sin^2 \theta_{\text{eff}}^{\text{lept}}$  with **FeynHiggs** 2.13.0 [28–31]. The SM contributions to the total decay width of the  $Z$  boson  $\Gamma_Z$  and the  $Z$  invisible width  $\Gamma_Z^{\text{inv}}$  were computed with **ZFITTER** 6.42 [32, 33] and those of the MSSM with **micrOMEGAs** 4.3.2 [34].  $\mathcal{L}_{\text{EWPO}}$ , Eq. (1), contains a Gaussian probability distribution function for each of these quantities, with central values and experimental and theoretical uncertainties added in quadrature (see Table IV):

$$\ln \mathcal{L}_{\text{EWPO}} = \ln \mathcal{L}_{M_W} + \ln \mathcal{L}_{\sin^2 \theta_{\text{eff}}^{\text{lept}}} + \ln \mathcal{L}_{\Gamma_Z} + \ln \mathcal{L}_{\Gamma_Z^{\text{inv}}}. \quad (1)$$

- **Flavour observables from B physics:** These include  $BR(B \rightarrow X_s \gamma)$ ,  $BR(B_s^0 \rightarrow \mu^+ \mu^-)$  and  $\frac{BR(B_u \rightarrow \tau \nu)}{BR(B_u \rightarrow \tau \nu)_{\text{SM}}}$  (Eq. 2). Theoretical predictions were calculated with **micrOMEGAs**. As in the previous case,  $\mathcal{L}_B$  includes Gaussian likelihoods for every B observable, with mean values and uncertainties given in Table IV:

$$\ln \mathcal{L}_B = \ln \mathcal{L}_{BR(B \rightarrow X_s \gamma)} + \ln \mathcal{L}_{BR(B_s^0 \rightarrow \mu^+ \mu^-)} + \ln \mathcal{L}_{\frac{BR(B_u \rightarrow \tau \nu)}{BR(B_u \rightarrow \tau \nu)_{\text{SM}}}}. \quad (2)$$

- **Constraints from the Higgs sector:**  $\mathcal{L}_{\text{Higgs}}$  accounts for the likelihood of the model predictions for the Higgs masses, branching ratios, production cross sections and total decay widths of the Higgs sector computed with **FeynHiggs** 2.13.0. These predictions were tested against exclusion bounds from Higgs searches at the LEP, Tevatron and LHC experiments using **HiggsBounds**

4.3.1 [35, 36] and HiggsSignals 1.4.0 [37].  $\mathcal{L}_{\text{Higgs}}$  also includes a Gaussian likelihood around the central value of the Higgs mass, the experimental and theoretical uncertainties considered here can be found in Table IV:

$$\ln \mathcal{L}_{\text{Higgs}} = \ln \mathcal{L}_{m_{h^0}} + \ln \mathcal{L}_{\text{Higgs sector}}. \quad (3)$$

- **LEP bounds on chargino and slepton masses:**  $m_{\tilde{\chi}_1^\pm}$ ,  $m_{\tilde{e}_R}$ ,  $m_{\tilde{\mu}_R}$ ,  $m_{\tilde{\tau}_1}$  and sneutrino mass constraints are incorporated in  $\mathcal{L}_{\text{LEP}}$ . Using the generic limits implemented in micrOMEGAs [38], smeared step-function likelihoods were constructed for each of them, at 95% CL, as in Ref. [39].

$$\ln \mathcal{L}_{\text{LEP}} = \ln \mathcal{L}_{m_{\tilde{\chi}_1^\pm}} + \ln \mathcal{L}_{m_{\tilde{e}_R}} + \ln \mathcal{L}_{m_{\tilde{\mu}_R}} + \ln \mathcal{L}_{m_{\tilde{\tau}_1}} + \ln \mathcal{L}_{m_{\tilde{\nu}}}. \quad (4)$$

- **LHC results on SUSY searches:** These were incorporated using SModelS 1.1.1 [40, 41]<sup>8</sup>, which employs upper limits and efficiency maps provided by the experimental collaborations. To properly estimate this likelihood, we first calculated the SUSY spectrum and decay widths with SOFTSUSY [42, 43], and the relevant SUSY cross sections at LO with micrOMEGAs. These cross sections were then improved with NLO+NLL contributions, using PYTHIA 8.2 [44, 45] and NLL-fast [46–52] for use by SModelS.  $\mathcal{L}_{\text{LHC}}$  accounts for SModelS computed likelihoods calculated for efficiency map results and smeared step-function likelihoods implemented for upper bounds at 95% CL as in the LEP case. We employed the most up-to-date SModelS and Fastlim 1.0 databases [53], which include 8 and 13 TeV results.
- **Dark matter (DM) relic abundance:** The value of  $\Omega_{\text{DM}} h^2$  was calculated with micrOMEGAs, and we implemented a Gaussian likelihood as for the previous constraints. See Table IV, for the corresponding experimental values.

Observable	Mean value	Standard deviation		Ref.
		experimental	theoretical	
$M_W$ (GeV)	80.385	0.015	0.01	[26]
$\sin^2 \theta_{\text{eff}}^{\text{lept}}$	0.231 53	0.000 16	0.0001	[54]
$\Gamma_Z$ (GeV)	2.4952	0.0023	0.001	[26, 55]
$\Gamma_Z^{\text{inv}}$ (GeV)	0.499	0.0015	0.001	[26]
$m_{h^0}$ (GeV)	125.09	0.24	2.0	[56]
$BR(B \rightarrow X_s \gamma) \times 10^4$	3.43	0.22	0.24	[57]
$BR(B_s^0 \rightarrow \mu^+ \mu^-) \times 10^9$	2.9	0.7	0.29	[58]
$\frac{BR(B_u \rightarrow \tau \nu)}{BR(B_u \rightarrow \tau \nu)_{\text{SM}}}$	1.04	0.34	-	[57, 59]
$\delta a_\mu^{\text{SUSY}} \times 10^{10}$	26.8	6.3	4.3	[26]
$\Omega_{\text{DM}} h^2$	0.1186	0.0010	0.012	[60]
Limits (95% CL)				Ref.
$m_{\tilde{\chi}_1^\pm}$	LEP2			[61]
$m_{\tilde{e}_R}, m_{\tilde{\mu}_R}, m_{\tilde{\tau}_1}$	LEP2			[62]
$m_{\tilde{\nu}}$	LEP2			[63]

TABLE IV. Experimental constraints used to implement the joint likelihood. Experimental uncertainties account for both systematic and statistical errors added in quadrature.

Now, let us describe the pMSSM-GA implementation. As mentioned in Section II, the fitness function was chosen to be the inverse of the chi-squared (as of course the GA seeks to maximise the

<sup>8</sup> Even though, the use of SModelS entails a set of underlying assumptions such as that only on-shell particles are considered in the cascade decay and virtual particles are replaced by an effective vertex, other tools available in the literature for the same purpose are less suited for extensive searches in multidimensional parameter spaces and for taking advantage of massive parallelism.



fitness). In detail, (for each model) first the input parameters were evolved from the GUT scale down to the electro-weak (EW) scale to compute the SUSY spectrum, branching ratios and decay widths using **SOFTSUSY**. Then, the Higgs sector was evaluated with **FeynHiggs**. Next, the DM relic abundance and the aforementioned observables were calculated as previously outlined. These data constitute the phenotype of each individual. Finally, the predictions were combined into a likelihood as in Eq. (5) to compute a total chi-squared and hence the fitness.

On a practical level, the value of the fitness function of each individual in a given population, which as mentioned in the Introduction is by far the most computationally intensive step of a GA, is of course independent for each individual, providing inherent parallelism and an opportunity to improve the performance of the heuristic search. To take advantage of this, we used the public parallel version of **PIKAIA 1.2** [64], which implements the Message Passing Interface (MPI) for a more efficient exploration of parameter space. Every package for the calculation of physical observables was modified accordingly and properly interfaced to **PIKAIA** to avoid data loss and disruption.

The number of individuals in a population,  $N_{\text{pop}}$ , was fixed to be 100. We explored a wide range of possibilities for the number of generations  $N_{\text{gen}}$ , and determined that for  $N_{\text{gen}} > 300$ , there was no significant improvement in the minimum  $\chi^2$ . In other words,  $N_{\text{gen}} = 300$  generations, and hence only  $N_{\text{pop}} \times N_{\text{gen}} = 3 \times 10^4$  evaluations of the fitness function, were sufficient to achieve a good convergence of the total  $\chi^2$ . (The number of times a model has to be evaluated is one of the best indicators of the overall efficiency gain: as mentioned earlier a useful point of comparison is the most rudimentary approach, namely a flat scan with just 2 points in each of the 23 dimensions, which would require  $10^7$  evaluations.)

The complete set of selected GA parameters is shown in Table I. Overall we performed 10 runs of this pMSSM-GA implementation, varying only the initial seed of the random number generator. The results did not change significantly between runs, or for longer runs.

### A. Muon Anomalous Magnetic Moment

The measured muon anomalous magnetic moment [65] shows a  $3.5\sigma$  deviation from the SM value, which could potentially be explained by supersymmetric contributions. The value of  $\delta a_\mu^{\text{SUSY}}$  for the MSSM was computed with **micrOMEGAs**, and the latest experimental average used from Ref. [26] (see Table IV) in a Gaussian probability distribution function,  $\mathcal{L}_{\delta a_\mu^{\text{SUSY}}}$ . Thus, the joint likelihood function reads,

$$\ln \mathcal{L}_{\text{Joint}} = \ln \mathcal{L}_{\text{EWPO}} + \ln \mathcal{L}_B + \ln \mathcal{L}_{\text{Higgs}} + \ln \mathcal{L}_{\text{LEP}} + \ln \mathcal{L}_{\text{LHC}} + \ln \mathcal{L}_{\Omega_{\text{DM}} h^2} + \ln \mathcal{L}_{\delta a_\mu^{\text{SUSY}}} . \quad (5)$$

### B. The Galactic Center Excess

For the later treatment of the Galactic Center Excess (GCE), we incorporated it into the joint likelihood as

$$\ln \mathcal{L}_{\text{Joint}} = \ln \mathcal{L}_{\text{EW}} + \ln \mathcal{L}_B + \ln \mathcal{L}_{\text{Higgs}} + \ln \mathcal{L}_{\text{LEP}} + \ln \mathcal{L}_{\text{LHC}} + \ln \mathcal{L}_{\Omega_{\text{DM}} h^2} + \ln \mathcal{L}_{\text{GCE}} . \quad (6)$$

Note that here we do not now take into account the likelihood from  $\delta a_\mu^{\text{SUSY}}$ .

To evaluate  $\chi_{\text{GCE}}^2$ , the procedure outlined in Ref. [66] was followed. That is we convoluted the differential photon spectrum of a given point of the parameter space with the energy resolution of the LAT instrument. We used the **P8REP-SOURCE-V6** total (front and back) resolution of the reconstructed incoming photon energy as a function of the energy for normally incident photons. Then  $\chi_{\text{GCE}}^2$  was calculated as follows [67]:

$$\chi_{\text{GCE}}^2 = \sum_{ij} \left( \frac{d\bar{N}}{dE_i}(\boldsymbol{\theta}) - \frac{dN}{dE_i} \right) \Sigma_{ij}^{-1} \left( \frac{d\bar{N}}{dE_j}(\boldsymbol{\theta}) - \frac{dN}{dE_j} \right), \quad (7)$$

where  $\Sigma_{ij}$  is the covariance matrix containing the statistical errors and the diffuse model and residual systematics obtained in Ref. [68] using the reprocessed Fermi-LAT Pass 8 data from 6.5 yr of



observations.  $dN/dE_i$  ( $d\bar{N}/dE_i$ ) stands for the measured (predicted) flux in the  $i$ th energy bin. The measured flux corresponds to the GCE spectrum from Ref. [69], derived using the Sample Model (see Section 2.2 of Ref. [69] for a complete description of this model). The vector  $\theta$  refers to the pMSSM parameters that determine the predicted photon flux.

## IV. RESULTS

### A. Muon Anomalous Magnetic Moment

In Fig.1, we represent the evolution of the minimum  $\chi^2$  (associated with the maximum fitness) as a function of the generation number for each of the ten runs. As already mentioned, the maximum fitness is a monotonically increasing function (due to the elitism), which results in a monotonically decreasing  $\chi^2$ . The evolution proceeds rapidly during the first iterations and stabilises after approximately 100 generations, with no apparent differences among the various runs.

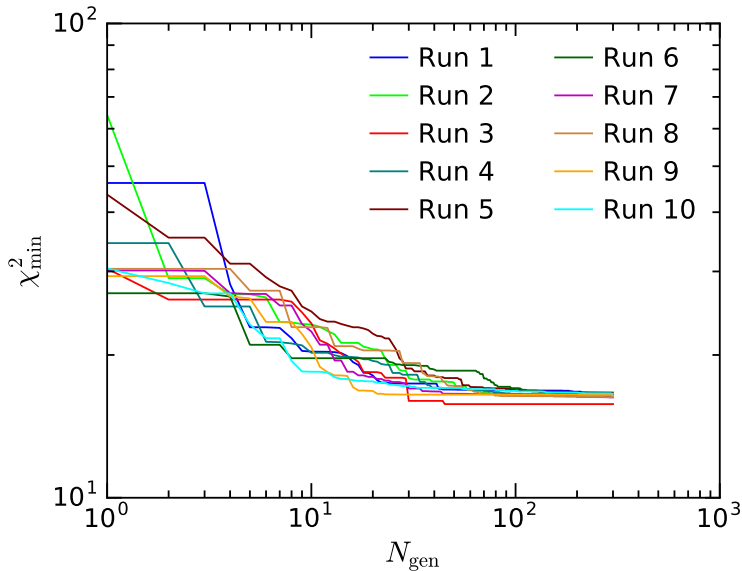


FIG. 1.  $\chi^2_{\min}$  vs. number of generations for the ten runs.

The goodness of the best-fit point for each run is shown in Table V, where we also include the contribution from each observable. The total  $\chi^2$  is of order  $\chi^2 \approx 16$  for the ten runs. The greatest contribution always comes from the muon anomalous magnetic moment ( $\chi^2_{\delta a_\mu^{\text{SUSY}}} \approx 12$ ), while the predictions for the other observables are in good agreement with the experimental results. For example, the combination of Higgs observables leads to  $\chi^2_{\text{HiggsSignals}} \approx 1.2$ . The fit to the invisible  $Z$ -width, which leads to  $\chi^2_{\Gamma_Z}$  is consistent with the SM prediction. There is an evident tension between the muon anomalous magnetic moment and the rest of the observables. A good fit to the latter is only possible at the expense of a very small supersymmetric contribution to  $a_\mu$ . Table VI shows the corresponding values of the observables for these best fit points, where we can observe that the resulting  $\delta a_\mu^{\text{SUSY}}$  is always two orders of magnitude smaller than the observed  $\delta a_\mu^{\text{SUSY}} = 26.8^{+6.3}_{-4.3} \times 10^{-10}$ . The tension between the observed value of the Higgs mass and the muon anomalous magnetic moment is well documented in the literature (see e.g. Ref. [70]).

The top plot of Fig. 2 shows the resulting SUSY spectrum for the particular case of run 3. The colour code is a visual aid to illustrate the evolution of the GA towards a final result. Blue corresponds to early generations, green to late ones, and the final generation, 300, is shown in yellow. The same colour map will be used throughout all the plots in this paper. Note that it is entirely expected

	Run 1	Run 2	Run 3	Run 4	Run 5	Run 6	Run 7	Run 8	Run 9	Run 10
$\chi^2_{\Omega_{\tilde{\chi}_1^0} h^2}$	0.0067	0.0044	0.0174	0.0002	0.0045	0.0035	0.0096	0.0021	0.0000	0.0020
$\chi^2_{\text{HiggsSignals}}$	1.2950	1.2983	1.1452	1.2899	1.2902	1.2914	1.1579	1.2811	1.2804	1.2995
$\chi^2_{m_{h^0}}$	0.1125	0.2174	0.0005	0.0921	0.0879	0.0782	0.3911	0.0656	0.1475	0.1331
$\chi^2_{M_W}$	0.1190	0.0350	0.0008	0.1006	0.2500	0.0223	0.0004	0.1642	0.1205	0.2239
$\chi^2_{\sin^2 \theta_{\text{eff}}^{\text{lept}}}$	0.1538	0.1463	0.1569	0.1575	0.1552	0.1665	0.1639	0.1601	0.1567	0.1470
$\chi^2_{\Gamma_Z}$	0.0332	0.0121	0.0001	0.0602	0.0388	0.1175	0.0102	0.0451	0.0362	0.0561
$\chi^2_{\Gamma_Z^{\text{inv}}}$	2.3054	2.3027	2.2842	2.3056	2.3045	2.3089	2.2998	2.3028	2.3003	2.3024
$\chi^2_{BR(B \rightarrow X_s \gamma)}$	0.0664	0.0741	0.0596	0.0911	0.0689	0.1050	0.1664	0.0929	0.0717	0.0761
$\chi^2_{BR(B_s^0 \rightarrow \mu^+ \mu^-)}$	0.1647	0.1818	0.1498	0.1707	0.1617	0.1623	0.1733	0.1888	0.1715	0.1593
$\chi^2_{\frac{BR(B_u \rightarrow \tau \nu)}{BR(\bar{B}_u \rightarrow \tau \nu)_{\text{SM}}}}$	0.0140	0.0143	0.0142	0.0143	0.0141	0.0140	0.0142	0.0154	0.0143	0.0140
$\chi^2_{\text{LEP}}$	0.0000	0.0000	0.0000	0.0000	0.0000	0.0000	0.0000	0.0000	0.0000	0.0000
$\chi^2_{\text{LHC}}$	0.0000	0.0000	0.0000	0.0000	0.0000	0.0000	0.0000	0.0000	0.0000	0.0000
$\chi^2_{\delta a_\mu^{\text{SUSY}}}$	12.2691	12.0273	11.9275	12.2113	12.2873	12.2926	11.8926	11.9721	12.1162	12.1683
$\chi^2_{\text{tot}}$	16.5398	16.3138	15.7562	16.4935	16.6631	16.5621	16.2793	16.2904	16.4152	16.5816

TABLE V. Contributions to the  $\chi^2$  of the best fit points. In blue, we show the leading contribution, which comes from the fit to the muon anomalous magnetic moment,  $\delta a_\mu^{\text{SUSY}}$ .

Observable	Run 1	Run 2	Run 3	Run 4	Run 5	Run 6	Run 7	Run 8	Run 9	Run 10
$m_{h^0}(\text{GeV})$	124.42	124.15	125.13	124.48	124.49	124.53	123.83	124.57	124.32	124.36
$M_W(\text{GeV})$	80.379	80.382	80.386	80.379	80.376	80.382	80.385	80.378	80.379	80.377
$\sin^2 \theta_{\text{eff}}^{\text{lept}}$	0.23146	0.23146	0.23146	0.23146	0.23146	0.23145	0.23145	0.23146	0.23146	0.23146
$\Gamma_Z(\text{GeV})$	2.4947	2.4949	2.4952	2.4946	2.4947	2.4943	2.4950	2.4947	2.4947	2.4946
$\Gamma_Z^{\text{inv}}(\text{GeV})$	0.5017	0.5017	0.5017	0.5017	0.5017	0.5017	0.5017	0.5017	0.5017	0.5017
$BR(B \rightarrow X_s \gamma) \times 10^4$	3.35	3.34	3.35	3.33	3.34	3.32	3.30	3.33	3.34	3.34
$BR(B_s^0 \rightarrow \mu^+ \mu^-) \times 10^9$	3.21	3.22	3.19	3.21	3.20	3.21	3.22	3.23	3.21	3.20
$\frac{BR(B_u \rightarrow \tau \nu)}{BR(\bar{B}_u \rightarrow \tau \nu)_{\text{SM}}}$	1.00	1.00	1.00	1.00	1.00	1.00	1.00	1.00	1.00	1.00
$\Omega_{\tilde{\chi}_1^0} h^2$	0.1178	0.1180	0.1204	0.1190	0.1180	0.1195	0.1200	0.1194	0.1188	0.1193
$\delta a_\mu^{\text{SUSY}} \times 10^{10}$	0.0827	0.3472	0.4572	0.1457	0.0063	0.0057	0.4958	0.4081	0.2497	0.1927

TABLE VI. Observable values for the best fit points. In blue, we display the results for  $\delta a_\mu^{\text{SUSY}}$ , which show a large discrepancy with the observed value.

that there will still be unfit individuals in the population exhibiting a large  $\chi^2$ . For this reason, a useful approach is to collate the best fit points from all the different runs. The bottom plot of Fig. 2 includes the information from all the ten runs, together with the corresponding best fit points. For convenience, these are also listed in Table VIII. As the population evolves, one can observe clustering around certain solutions. Whereas the best fit points seem to favour specific ranges of masses in the lightest neutralino and chargino, they appear more spread in the squark and slepton sector. A pattern emerges where  $m_{\tilde{\chi}_1^0} \approx m_{\tilde{\chi}_1^\pm} \approx 2$  TeV, the squark masses are generally above 6 TeV (except for the lightest stop, for which  $m_{\tilde{t}_1} \approx 2 - 3$  TeV), and slepton masses show a wide range of variation 2 – 10 TeV. For completeness, the pMSSM input parameters (19 soft supersymmetry-breaking terms and four nuisance parameters) for the best fit points of each run are listed in Table VII.

Parameter	Run 1	Run 2	Run 3	Run 4	Run 5	Run 6	Run 7	Run 8	Run 9	Run 10
SM										
$[\alpha_{\text{EM}}(M_Z)^{\overline{MS}}]^{-1}$	128.0152	128.0177	128.0127	128.0171	128.0161	128.0167	128.0119	128.0138	128.0119	128.0161
$\alpha_S(M_Z)^{\overline{MS}}$	0.1171	0.1174	0.1183	0.1169	0.1171	0.1164	0.1175	0.1170	0.1171	0.1168
$m_b(\text{GeV})$	4.5417	4.5560	4.7420	4.5973	4.5680	4.5552	4.5468	4.5943	4.5403	4.5407
$m_t(\text{GeV})$	175.4984	175.4853	175.3661	175.4839	175.4868	175.4799	175.4380	175.4675	175.4268	175.4351
pMSSM (GUT scale)										
$M_1(\text{TeV})$	9.5703	9.7113	3.9085	7.5518	5.7486	8.6224	7.4272	7.8098	9.2195	6.2369
$M_2(\text{TeV})$	2.5890	2.4750	2.1502	2.5057	2.6390	2.6583	2.2613	2.2840	2.4634	2.6338
$M_3(\text{TeV})$	3.2780	2.2800	1.1040	3.2561	4.0505	3.1197	1.3771	2.1184	2.4783	4.0718
$m_{H_u}(\text{TeV})$	1.6667	1.3993	4.1690	5.8189	5.0971	2.2366	0.3387	6.8716	0.9580	6.3635
$m_{H_d}(\text{TeV})$	7.1708	5.2775	8.2714	1.1057	6.3784	8.0392	6.9334	1.6798	3.1264	7.2671
$m_{\tilde{Q}_3}(\text{TeV})$	4.7038	4.9000	9.0737	7.0818	5.8858	5.9333	2.2149	6.0595	5.8636	6.6930
$m_{\tilde{Q}_{1,2}}(\text{TeV})$	5.3936	7.6163	3.6165	8.0554	4.6423	9.7422	4.8321	1.0849	7.1282	9.5621
$m_{\tilde{U}_3}(\text{TeV})$	0.1784	3.9889	6.6280	2.1355	1.9408	3.0753	4.0231	4.4181	3.1066	0.6947
$m_{\tilde{U}_{1,2}}(\text{TeV})$	1.4621	2.2405	8.0701	4.2783	6.5618	7.0730	1.6677	1.5040	6.5059	6.8387
$m_{\tilde{D}_3}(\text{TeV})$	0.7708	0.4281	5.4714	7.2873	1.4363	0.3643	0.1945	0.0882	1.8254	0.7754
$m_{\tilde{D}_{1,2}}(\text{TeV})$	0.1395	4.1474	7.2591	0.4960	3.9536	3.1839	0.7612	0.9395	1.3482	5.1211
$m_{\tilde{L}_3}(\text{TeV})$	6.7797	8.9868	4.8607	8.7979	7.6243	9.8535	7.6822	6.3356	7.6277	8.3796
$m_{\tilde{L}_{1,2}}(\text{TeV})$	7.5105	0.8366	2.6651	4.1286	9.0621	8.6661	1.0870	1.7923	1.6668	3.3159
$m_{\tilde{E}_3}(\text{TeV})$	1.3255	4.6784	3.1272	3.3281	0.7113	4.5917	8.9473	6.9846	7.7331	3.0309
$m_{\tilde{E}_{1,2}}(\text{TeV})$	9.4672	1.2755	1.8426	8.3371	9.0375	9.8130	1.1521	5.6990	6.7869	5.9095
$A_t(\text{TeV})$	-9.4740	-9.8184	-9.6588	-9.9870	-9.9878	-9.7382	-7.3392	-9.3542	-9.8716	-9.6492
$A_b(\text{TeV})$	-7.7118	-6.1908	8.5946	0.3908	9.4784	-6.1000	-1.2494	-2.1864	2.3702	-1.1100
$A_\tau(\text{TeV})$	8.6880	6.2710	-6.5096	-0.0063	-9.9068	-0.9948	8.6904	8.9710	-9.2448	-1.9952
$\tan \beta$	22.6238	29.3282	28.4906	21.5324	19.4162	18.4574	26.7140	22.5170	24.8102	20.9054

TABLE VII. Input parameters for the best fit points.

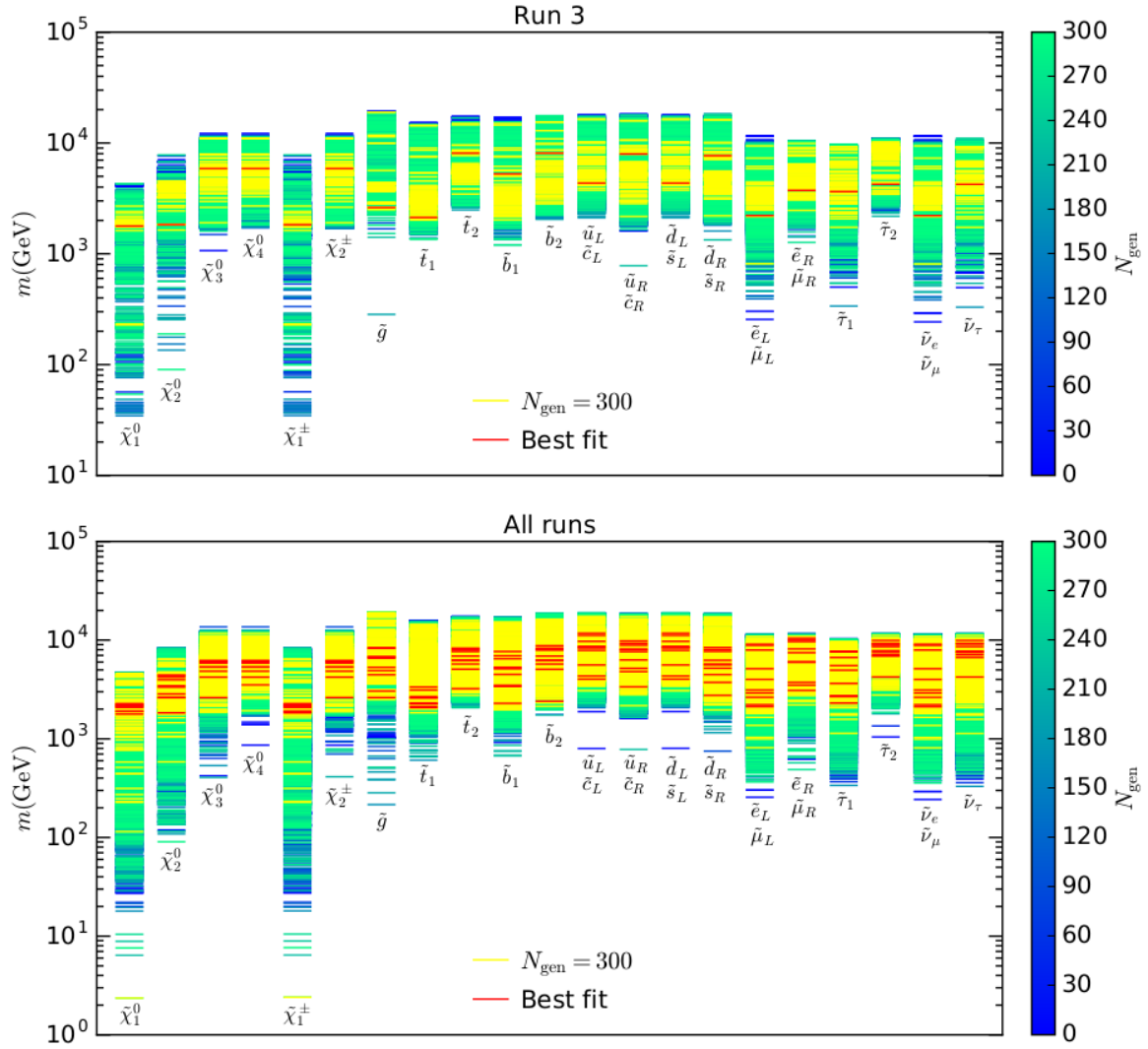


FIG. 2. (Top) SUSY spectrum for all the generations in run 3. Yellow represents the results for the last generation and the red line corresponds to the best fit point. (Bottom) The same, but including the results for the ten runs.

m(TeV)	Run 1	Run 2	Run 3	Run 4	Run 5	Run 6	Run 7	Run 8	Run 9	Run 10
$m_{\tilde{\chi}_1^0}$	2.1899	2.1016	1.7779	2.1262	2.2249	2.2701	1.8967	1.9043	2.0891	2.2252
$m_{\tilde{\chi}_2^0}$	4.3778	4.4140	1.8323	3.4508	2.6267	3.9700	3.3381	2.6099	4.2132	2.8475
$m_{\tilde{\chi}_3^0}$	6.0329	5.8963	5.8774	5.3433	5.3503	6.1583	4.2183	2.6122	6.2057	4.8463
$m_{\tilde{\chi}_4^0}$	6.0340	5.8975	5.8779	5.3444	5.3512	6.1593	4.2205	3.5199	6.2066	4.8475
$m_{\tilde{\chi}_1^\pm}$	2.1901	2.1017	1.8308	2.1264	2.2250	2.2702	1.8968	1.9045	2.0893	2.2254
$m_{\tilde{\chi}_2^\pm}$	6.0341	5.8974	5.8784	5.3446	5.3516	6.1595	4.2200	2.6147	6.2067	4.8478
$m_{\tilde{g}}$	6.7304	4.9071	2.6147	6.8046	8.2574	6.5645	3.0447	4.4649	5.3003	8.3863
$m_{\tilde{t}_1}$	3.1168	3.3535	2.1280	2.2745	2.5939	2.6113	2.2757	2.0702	2.2747	2.6774
$m_{\tilde{t}_2}$	6.2486	5.0756	8.1006	7.6622	7.9175	6.8952	3.2181	5.7306	6.2510	8.2790
$m_{\tilde{b}_1}$	5.2788	3.4830	5.2605	7.6589	6.9380	5.1184	2.2860	3.3888	4.4942	6.4800
$m_{\tilde{b}_2}$	6.2432	5.0657	8.0991	8.7702	7.9142	6.8912	2.4021	5.7259	6.2467	8.2761
$m_{\tilde{u}_L}$	7.8708	8.6567	4.3350	9.7225	8.4026	11.1512	5.6043	4.0216	8.3820	11.7328
$m_{\tilde{u}_R}$	6.3070	5.1789	7.9673	7.6343	9.2697	8.8657	3.3666	4.7984	8.1069	9.7987
$m_{\tilde{d}_L}$	7.8711	8.6569	4.3356	9.7226	8.4029	11.1513	5.6047	4.0222	8.3822	11.7329
$m_{\tilde{d}_R}$	5.6090	5.7292	7.6764	5.1876	8.0160	6.2496	2.7580	3.7299	4.4788	8.4131
$m_{\tilde{e}_L}$	7.8708	8.6566	4.3349	9.7224	8.4026	11.1511	5.6042	4.0216	8.3819	11.7327
$m_{\tilde{e}_R}$	6.3070	5.1789	7.9673	7.6343	9.2697	8.8657	3.3666	4.7984	8.1069	9.7986
$m_{\tilde{s}_L}$	7.8710	8.6568	4.3355	9.7226	8.4028	11.1513	5.6046	4.0222	8.3822	11.7329
$m_{\tilde{s}_R}$	5.6088	5.7290	7.6763	5.1875	8.0159	6.2495	2.7577	3.7299	4.4787	8.4130
$m_{\tilde{\tau}_1}$	2.6846	4.9582	3.6410	2.3003	2.6804	5.5212	7.5905	6.6731	7.7304	2.7379
$m_{\tilde{\tau}_2}$	7.0855	9.1210	4.2356	9.2520	7.4738	9.9211	8.8642	6.8868	7.8166	8.5809
$m_{\tilde{\nu}_L}$	7.9354	2.6358	2.2153	5.1338	9.0696	8.8432	2.1177	3.1214	2.9146	4.0030
$m_{\tilde{\nu}_R}$	9.9813	3.4901	3.7335	8.1401	9.6424	10.4569	3.0946	5.9648	7.4653	6.0597
$m_{\tilde{\mu}_L}$	7.9348	2.6351	2.2140	5.1334	9.0692	8.8428	2.1168	3.1210	2.9139	4.0025
$m_{\tilde{\mu}_R}$	9.9803	3.4891	3.7320	8.1396	9.6416	10.4562	3.0934	5.9644	7.4648	6.0590
$m_{\tilde{\nu}_e}$	7.9347	2.6343	2.2136	5.1329	9.0689	8.8425	2.1160	3.1201	2.9132	4.0019
$m_{\tilde{\nu}_\mu}$	7.9341	2.6336	2.2123	5.1325	9.0685	8.8421	2.1151	3.1197	2.9125	4.0014
$m_{\tilde{\nu}_\tau}$	7.0855	9.1202	4.2321	9.2513	7.4730	9.9204	7.5898	6.6725	7.7339	8.5802
$m_{H^0}$	9.2213	7.6930	9.1800	5.8055	7.9619	9.9571	7.8982	3.4162	6.9123	8.6629
$m_{A^0}$	9.2205	7.6926	9.1809	5.8055	7.9620	9.9566	7.8985	3.4162	6.9121	8.6630
$m_{H^\pm}$	9.2210	7.6931	9.1791	5.8061	7.9624	9.9571	7.8992	3.4172	6.9126	8.6634

TABLE VIII. SUSY spectrum for the best fit points (represented by red lines in Fig. 2).

Let us discuss the results more in detail. We will use run 3 as an example, but the results for other runs are qualitatively similar.

First, it is clear that the dark matter relic density is one of the main drivers of the evolution of the fitness function, as we can see from the right panel of Fig. 3, which shows the correlation between the total  $\chi^2$  and  $\chi_{\Omega_{\tilde{\chi}_1^0}^2 h^2}^2$ . This is due to the high precision of the observed value of the dark matter relic abundance, but also to the fact that the relic density of the neutralino is in general very large. In order to reproduce the observed value, resonant annihilation (generally through the pseudoscalar Higgs, when  $2m_{\tilde{\chi}_1^0} \approx m_{A^0}$ ) or coannihilation with the next-to-lightest supersymmetric particle (NLSP) is required [71]. The flexible structure of the pMSSM allows for various forms of coannihilation, where the NLSP can be either the lightest stau [72, 73], the lightest stop [74–76], electroweakinos (such as the second lightest neutralino or the lightest chargino) [77–81]. The latter can occur in the so-called focus point region, where both the neutralino and chargino are 1 TeV Higgsino-like particles [82, 83] or 2 – 3 TeV wino-like particles [84]. The choice of non-universal soft parameters at the GUT scale [85] facilitates obtaining these various solutions, contrary to more constrained scenarios such as the CMSSM.

The values of the wino soft mass parameter at the GUT scale,  $M_2 \approx 2.5$  TeV (see Table VII) and the hierarchy of the gaugino masses  $M_2 < M_3 < M_1$  ensure that the lightest neutralino and the lightest chargino are both wino-like and with very similar masses (degenerate to order 1%). This facilitates coannihilation effects, without introducing a large fine-tuning in the dark matter sector [86], and is the clearest characteristic of all the runs. The composition of the lightest neutralino is shown in Fig. 4, clearly showing that the last generation corresponds to wino-like neutralino, with a subleading Higgsino component. The GUT values of the gaugino mass parameters are represented in Fig. 14. This feature occurs for all the runs. It is well known, from previous studies in non-universal SUSY models [82, 83], that a wino-like neutralino can have the correct relic abundance for a range of masses around 2 – 3 TeV.

The final generations of all the runs cluster around the observed value of the dark matter relic abundance, as the left panel of Fig. 3 shows. Satisfying the dark matter relic density while fulfilling all the other experimental constraints requires in general a careful choice of the initial parameters, only possible in narrow bands of the parameter space. Finding these solutions in scans of the parameter space is therefore very costly, and it is here that the GA excels, by the population quickly condensing on the relevant subspaces. It is indeed remarkable how easily these are obtained by a GA, requiring a relatively small number of generations. As we mentioned, each of the runs required approximately  $10^4$  model evaluations. Refs. [21, 87] concluded that evolutionary algorithms can outperform Bayesian inference tools even in relatively low dimensional models such as the CMSSM, but we find here that in broader models such as the pMSSM they become orders of magnitude more efficient.

It is indeed interesting to compare these results in more detail with the previous GA scans performed in the context of the Constrained version of MSSM (CMSSM) [21], which only contains five free parameters and in which gaugino masses are assumed to be universal at the GUT scale. In that case, after applying the corresponding RGEs, one obtains  $M_2 > M_1$  at low-energy. Thus, the lightest neutralino cannot be wino-like, and instead, the best fit point is obtained for Higgsino-like neutralinos (with an approximate mass of 1 TeV).

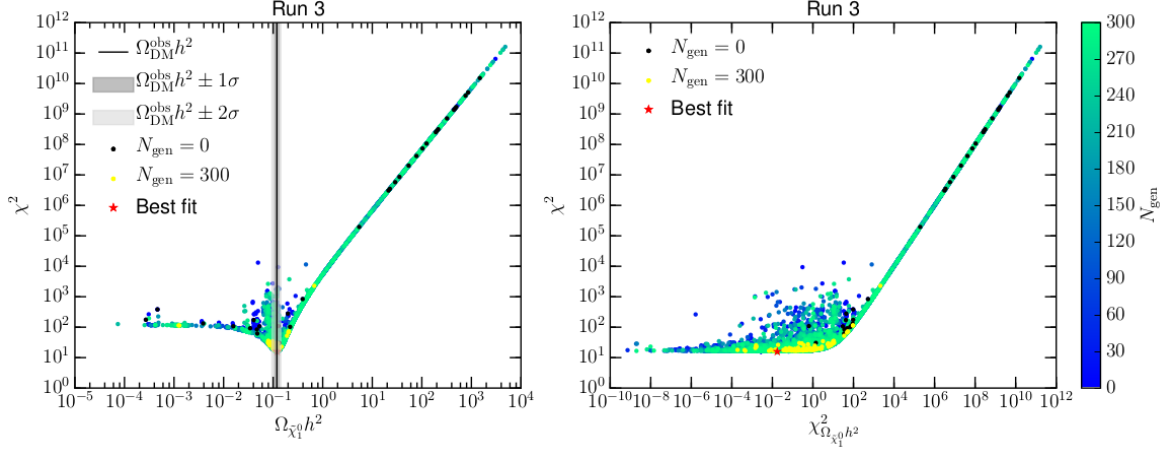


FIG. 3. Left:  $\chi^2$  vs.  $\Omega_{\tilde{\chi}_1^0} h^2$ . The solid black line corresponds to the  $\Omega_{\text{DM}} h^2$  mean value, see Table IV. As a reference, we show the  $1\sigma$  and  $2\sigma$  regions around the mean value in grey and light grey, respectively. Right:  $\chi^2$  vs.  $\chi_{\Omega_{\tilde{\chi}_1^0} h^2}^2$ . The colour map denotes the evolution from number from generation 0 up to 300, the initial guesses ( $N_{\text{gen}} = 0$ ) are depicted in black and the final generation ( $N_{\text{gen}} = 300$ ) in yellow. The red star corresponds to the best fit.

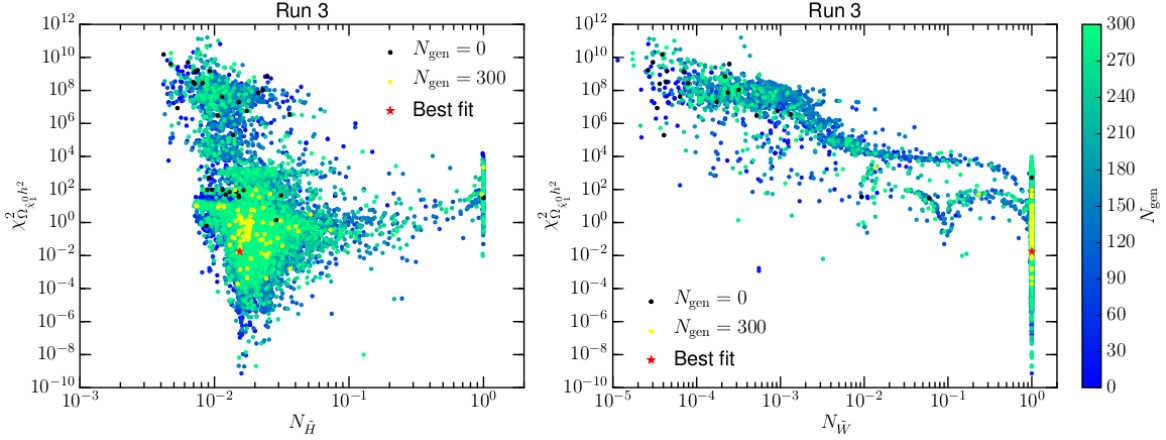


FIG. 4.  $\chi_{\Omega_{\tilde{\chi}_1^0} h^2}^2$  vs. the Higgsino (left) and wino (right) component of the lightest neutralino.

A wino-like neutralino is not particularly easy to find through direct detection techniques (as the elastic scattering cross section with nuclei is generally dominated by Higgs exchange diagrams which are enhanced by the Higgsino component). In Fig. 5, we show the predicted contribution to the spin-independent (SI) and spin-dependent (SD) scattering cross section for all the different runs and in Table IX we include the values obtained for the best fit points. Note that these plots only include points with  $\Omega_{\tilde{\chi}_1^0} h^2 \leq \Omega_{\text{DM}} h^2 + 1\sigma$ : solutions with  $\Omega_{\tilde{\chi}_1^0} h^2 < \Omega_{\text{DM}} h^2$  have been weighted by  $\xi = \min[1, \Omega_{\tilde{\chi}_1^0} h^2 / \Omega_{\text{DM}} h^2]$  as indicated in each panel. It is interesting to observe that all the best fit points are nicely grouped around the same solution, with  $\sigma_{\tilde{\chi}_1^0 p}^{\text{SI}} \approx 10^{-11}$  pb and  $m_{\tilde{\chi}_1^0} \approx 2$  TeV. This is just below the projected sensitivity of LZ and potentially within the reach of the planned Darwin experiment. Notice, however, that it is extremely close to the region where the background due to coherent neutrino scattering becomes important. The spin-dependent contribution is negligible for these points. Regarding indirect detection, the predicted thermal averaged annihilation cross section at zero velocity is also shown in this table. It is of the order of  $\langle \sigma v \rangle_0 \approx 10^{-26} \text{ cm}^3 \text{ s}^{-1}$ , just within the



reach of the future CTA [88], as we can see in the lower panel of Fig. 5.

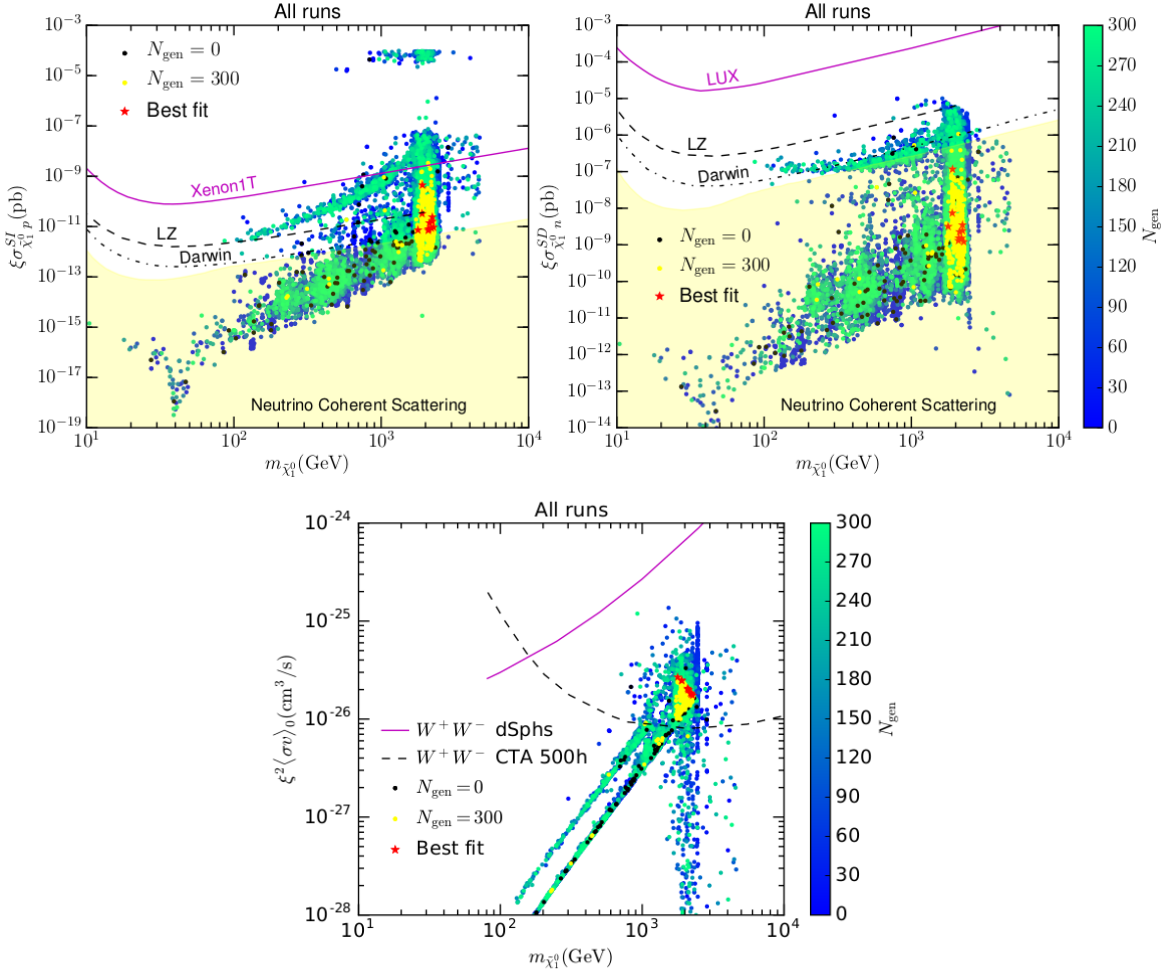


FIG. 5. Top left: Theoretical predictions for  $\xi\sigma_{\tilde{\chi}_1^0 p}^{SI}$  as a function of  $m_{\tilde{\chi}_1^0}$  for all the runs. Top right: Predictions for  $\xi\sigma_{\tilde{\chi}_1^0 n}^{SD}$  vs.  $m_{\tilde{\chi}_1^0}$ . The solid violet lines represent the leading constraint on SI and SD interactions from XENON1T [89] and LUX [90], respectively. The dashed and dot-dashed lines correspond to the sensitivity projections for LUX-ZEPLIN (LZ) [91] and DARWIN [92]. As a reference, we also show the irreducible neutrino background for a xenon target in yellow for SI (proton) and SD (neutron) cross sections [93]. Bottom: Thermally averaged neutralino annihilation cross section in the Galactic halo,  $\xi^2 \langle \sigma v \rangle_0$ , as a function of the lightest neutralino mass. The upper bound on  $\langle \sigma v \rangle_0$  for the  $W^+W^-$  annihilation channel derived from an analysis of 15 dwarf spheroidal (dSph) galaxies using the Fermi-LAT Pass 8 reprocessed data set [94] is depicted in violet. The dashed line corresponds to the expected sensitivity of CTA for the same annihilation channel [88].

The Higgs sector is of course another important source of constraints. The Higgs boson mass is properly recovered and, as Fig. 6 shows, it is an important influence in the evolution of the likelihood. The final population of models is grouped around the observed value. In contrast, the resulting  $\chi_{\text{HiggsSignals}}^2$  is always smaller than 2, which shows that the values of the Higgs couplings are never too far from the observed experimental values (compatible with the SM Higgs) and are thus not relevant in minimising the total  $\chi^2$ . In general, the predicted Higgs mass in the pMSSM is below the observed value, and in order to maximise the one-loop contributions, the stop trilinear coupling has to lead to maximal LR mixing in the stop mass matrix [95–98]. The GUT values of these quantities for the best fit points (Table VII) are such that this relation is fulfilled at low energy. This pushes  $A_t$  to large

	$\sigma_{\tilde{\chi}_1^0 p}^{SI}$ (pb)	$\sigma_{\tilde{\chi}_1^0 n}^{SI}$ (pb)	$\sigma_{\tilde{\chi}_1^0 p}^{SD}$ (pb)	$\sigma_{\tilde{\chi}_1^0 n}^{SD}$ (pb)	$\langle\sigma v\rangle_0$ (cm <sup>3</sup> s <sup>-1</sup> )
Run 1	$8.77 \times 10^{-12}$	$8.95 \times 10^{-12}$	$1.05 \times 10^{-9}$	$1.53 \times 10^{-9}$	$1.87 \times 10^{-26}$
Run 2	$8.07 \times 10^{-12}$	$8.23 \times 10^{-12}$	$1.23 \times 10^{-9}$	$1.55 \times 10^{-9}$	$2.04 \times 10^{-26}$
Run 3	$7.24 \times 10^{-12}$	$7.40 \times 10^{-12}$	$3.70 \times 10^{-10}$	$3.16 \times 10^{-9}$	$2.68 \times 10^{-26}$
Run 4	$1.39 \times 10^{-11}$	$1.42 \times 10^{-11}$	$2.18 \times 10^{-9}$	$2.27 \times 10^{-9}$	$1.99 \times 10^{-26}$
Run 5	$1.60 \times 10^{-11}$	$1.63 \times 10^{-11}$	$2.11 \times 10^{-9}$	$2.45 \times 10^{-9}$	$1.81 \times 10^{-26}$
Run 6	$9.30 \times 10^{-12}$	$9.48 \times 10^{-12}$	$1.15 \times 10^{-9}$	$1.22 \times 10^{-9}$	$1.75 \times 10^{-26}$
Run 7	$3.24 \times 10^{-11}$	$3.30 \times 10^{-11}$	$5.32 \times 10^{-9}$	$7.38 \times 10^{-9}$	$2.50 \times 10^{-26}$
Run 8	$4.45 \times 10^{-10}$	$4.54 \times 10^{-10}$	$1.12 \times 10^{-7}$	$1.17 \times 10^{-7}$	$2.46 \times 10^{-26}$
Run 9	$7.01 \times 10^{-12}$	$7.15 \times 10^{-12}$	$9.36 \times 10^{-10}$	$1.30 \times 10^{-9}$	$2.06 \times 10^{-26}$
Run 10	$2.38 \times 10^{-11}$	$2.43 \times 10^{-11}$	$3.88 \times 10^{-9}$	$3.50 \times 10^{-9}$	$1.81 \times 10^{-26}$

TABLE IX. Predictions for DM direct and indirect detection observables for the best fit points of the ten runs

values, whereas  $\tan\beta \approx 20$  is favoured, as we can see in Fig. 8. The best fit points feature typical values of the  $\mu$  parameter in the range of 5 – 6 TeV, which leads to an EW fine-tuning of the order of thousands [99].

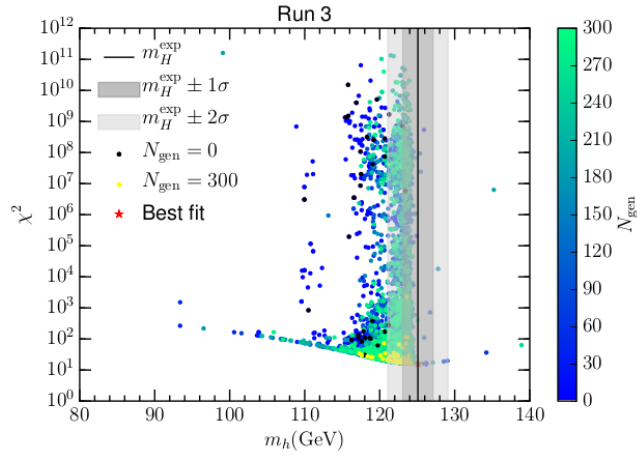
FIG. 6.  $\chi^2$  vs. Higgs mass. As a reference, we show the  $m_{h^0}$  mean value (solid black line), the  $1\sigma$  (grey) and  $2\sigma$  (light grey) regions, see Table IV for the exact values.

Figure 9 contains the fit to EW observables. We can see that both  $M_W$  and  $\sin^2\theta_{\text{eff}}^{\text{lept}}$  have an important influence on the fitness function. All these observables are properly reproduced in the final generation of points. The  $Z$  boson invisible width is only due to decay into neutrinos, as the neutralino mass is in general very large, and therefore compatible with that of the SM.

Finally, the goodness of the fit to the muon anomalous magnetic moment is shown in Fig. 10. It is evident from this plot that the observed value of  $\delta a_\mu^{\text{SUSY}}$  is not properly reproduced and that  $\delta a_\mu^{\text{SUSY}} \lesssim 10^{-10}$  throughout the whole evolution (which is almost equivalent to having just the SM contribution). The supersymmetric contribution to this observable is very small, thus resulting in a  $3\sigma$  discrepancy with respect to the observed value, and  $\chi_{\delta a_\mu^{\text{SUSY}}}^2 \approx 12$  for all the points. As we can see in the right-hand side plot in Fig. 10,  $\delta a_\mu^{\text{SUSY}}$  has no impact in the GA evolution and  $\chi_{\delta a_\mu^{\text{SUSY}}}^2$  does not vary through the different generations<sup>9</sup>. This may seem counterintuitive but is in fact a general

<sup>9</sup> Notice that, as the  $\mu$ -term is taken to be positive,  $\delta a_\mu^{\text{SUSY}}$  is positive and always adds to the SM contribution. Thus, the fit is always marginally better than the SM discrepancy with the observed experimental value.

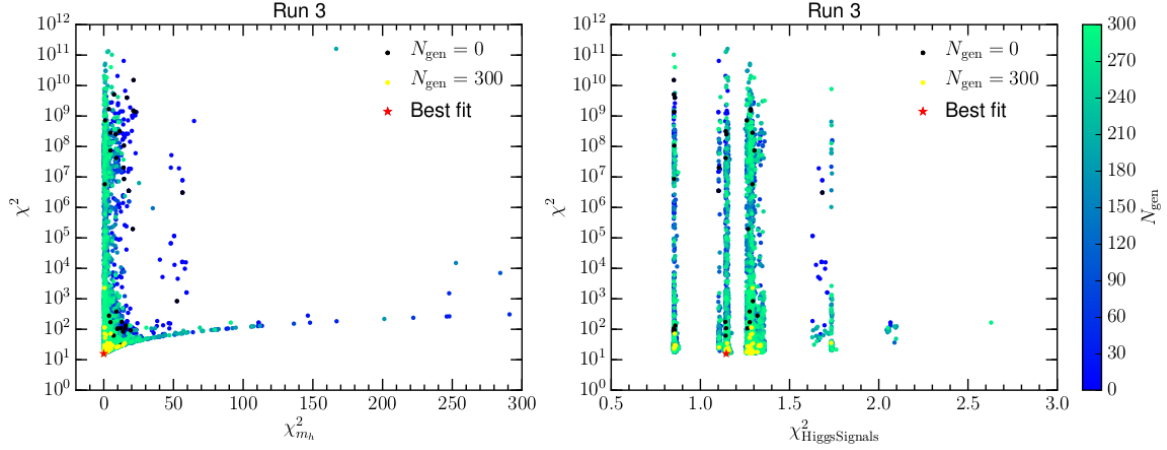


FIG. 7. Left:  $\chi^2_{\min}$  vs.  $\chi^2_{m_{h0}}$ . Right:  $\chi^2$  vs.  $\chi^2_{\text{HiggsSignals}}$ .

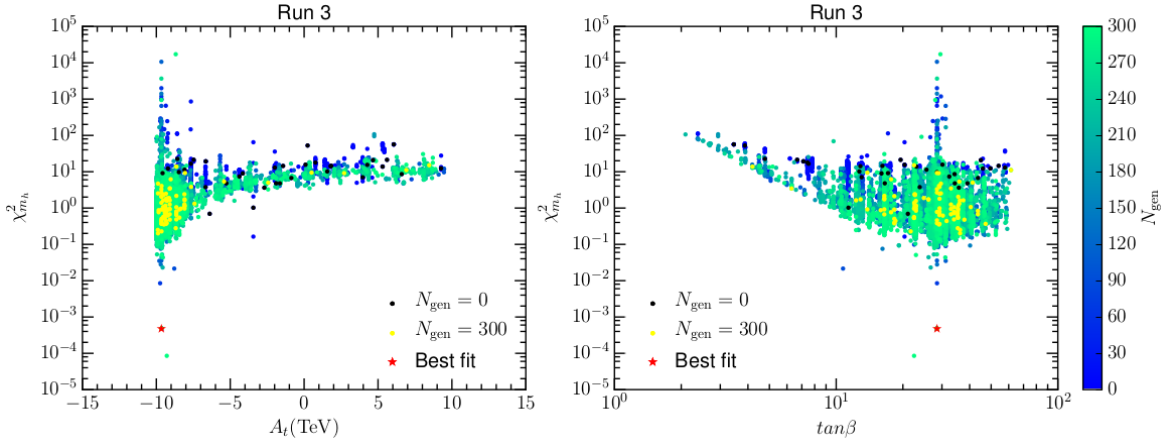


FIG. 8. Left:  $\chi^2_{m_{h0}}$  vs.  $A_t$ . Right:  $\chi^2_{m_{h0}}$  vs.  $\tan \beta$ .

expectation: attempting to fit this observable would degrade the fitness of the population much more than ignoring it altogether. Consequently the fitness of the entire population is degraded equally by including it in the likelihood, but the *relative* fitness (which is what determines the evolution) is relatively unaffected. We conclude that this observable simply cannot be fit within the model without severely degrading the  $\chi^2$ .

These results evidence the well-known tension between the muon anomalous magnetic moment and the rest of the observables. Whereas the former requires a light spectrum (in particular, light sleptons and neutralinos or charginos), LHC bounds and the value of the Higgs mass favour much heavier supersymmetric particles. There are very many LHC constraints, and in fact calculating them is the most costly part of determining the likelihood and hence fitness of a particular model.

In contrast, other observables, such as  $BR(B_s^0 \rightarrow \mu^+ \mu^-)$  are properly recovered, and in fact, contribute to minimising the total  $\chi^2$ , as shown in the left-hand side of Fig. 11 ( $BR(B \rightarrow X_s \gamma)$  and  $\frac{BR(B_u \rightarrow \tau \nu)}{BR(B_u \rightarrow \tau \nu)_{\text{SM}}}$ , shown in the middle and right panels of Fig. 11, are in general in very good agreement with the experimental result). Although we have used run 3 as an example, it should be pointed out that the other runs produce similar results.

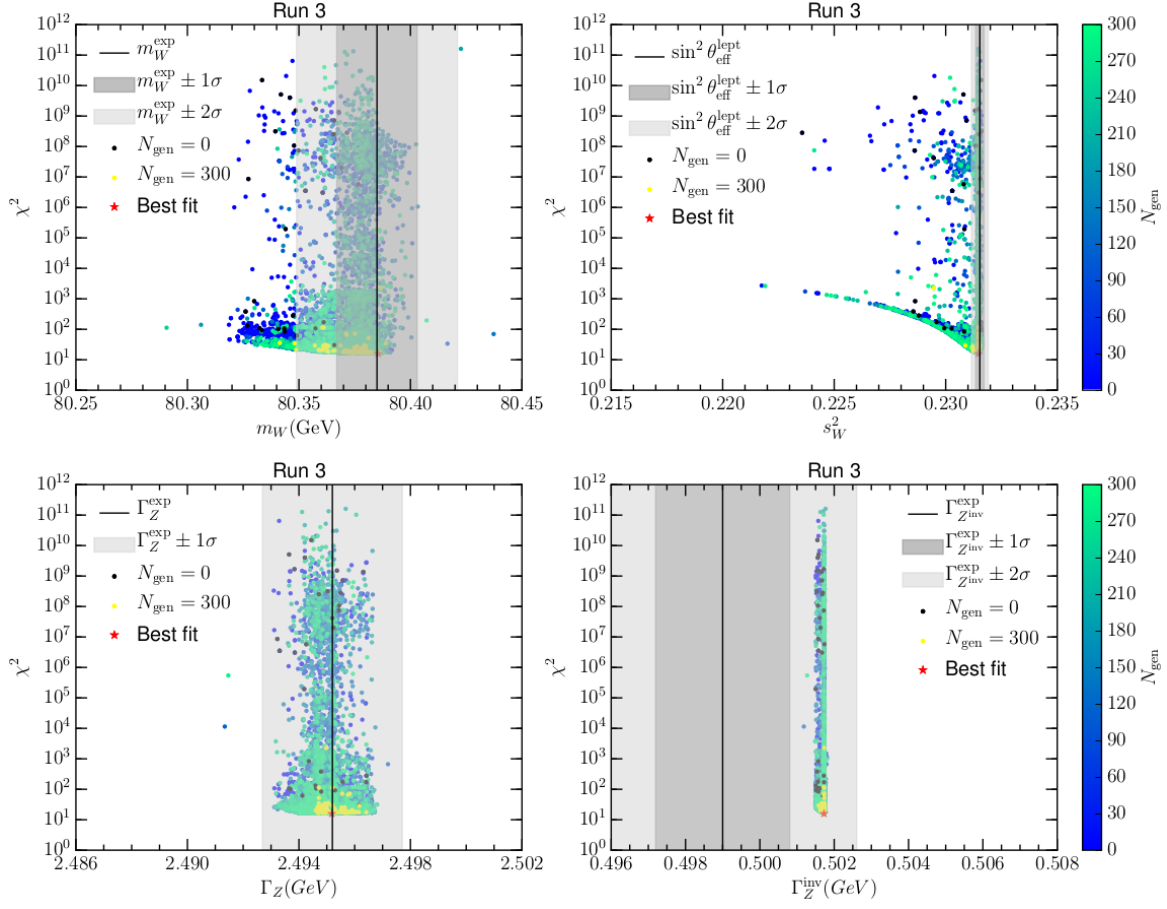


FIG. 9. Electroweak observables: Left:  $\chi^2$  vs.  $M_W$ . Right:  $\chi^2$  vs.  $\sin^2 \theta_{\text{eff}}^{\text{lept}}$ . Left:  $\chi^2$  vs.  $\Gamma_Z$ . Right:  $\chi^2$  vs.  $\Gamma_Z^{\text{inv}}$ . The solid black line corresponds to the mean value of each observable, and the shaded areas to the  $1\sigma$  (grey) and  $2\sigma$  (light grey) regions around that value according to Table IV.

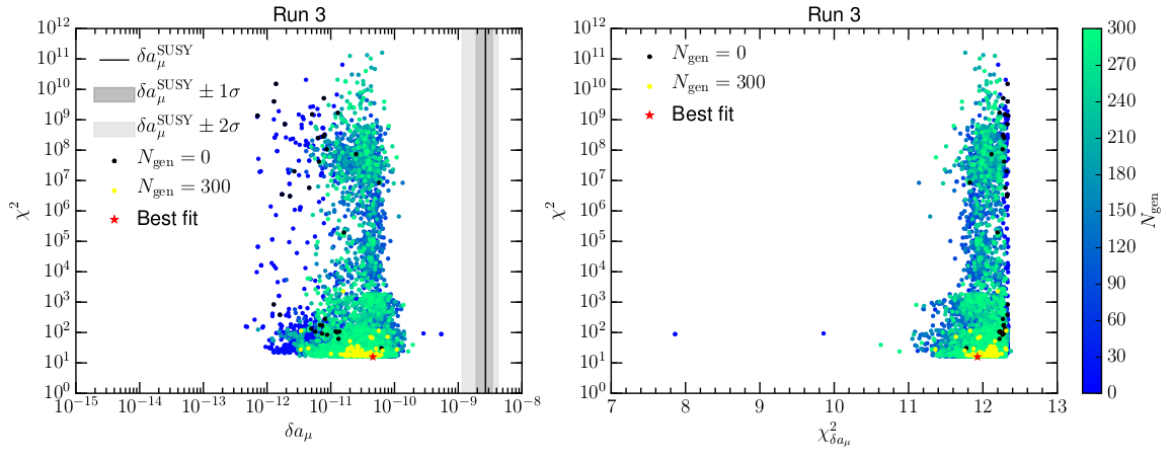


FIG. 10. Left:  $\chi^2$  vs.  $\delta a_\mu^{\text{SUSY}}$ . The solid black line corresponds to the  $\delta a_\mu^{\text{SUSY}}$  mean value, see Table IV. The  $1\sigma$  and  $2\sigma$  regions (light grey) around the mean value are shaded in grey and light grey, respectively. Right:  $\chi^2$  vs.  $\chi^2_{\delta a_\mu^{\text{SUSY}}}$ .

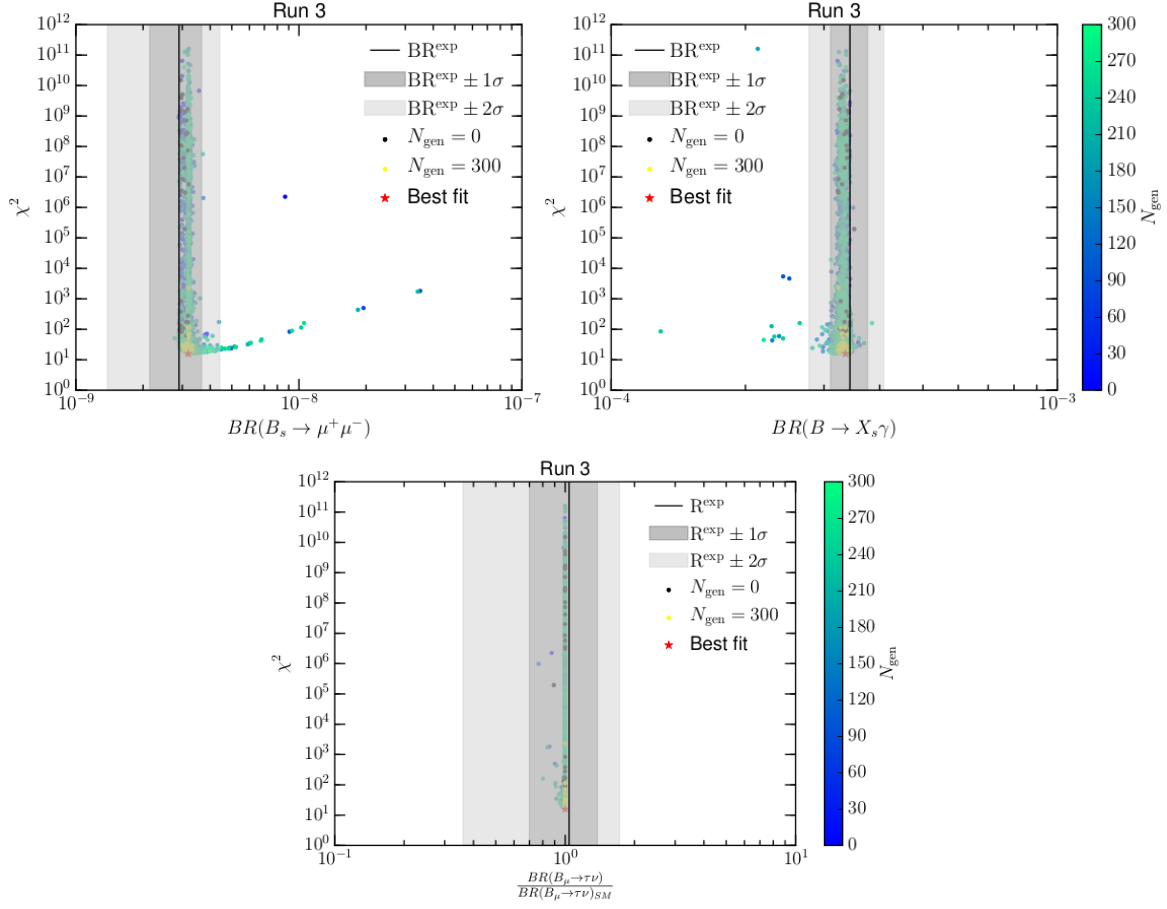
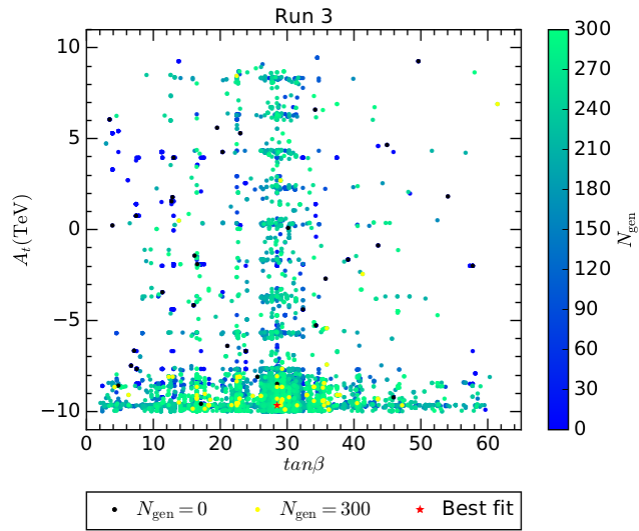
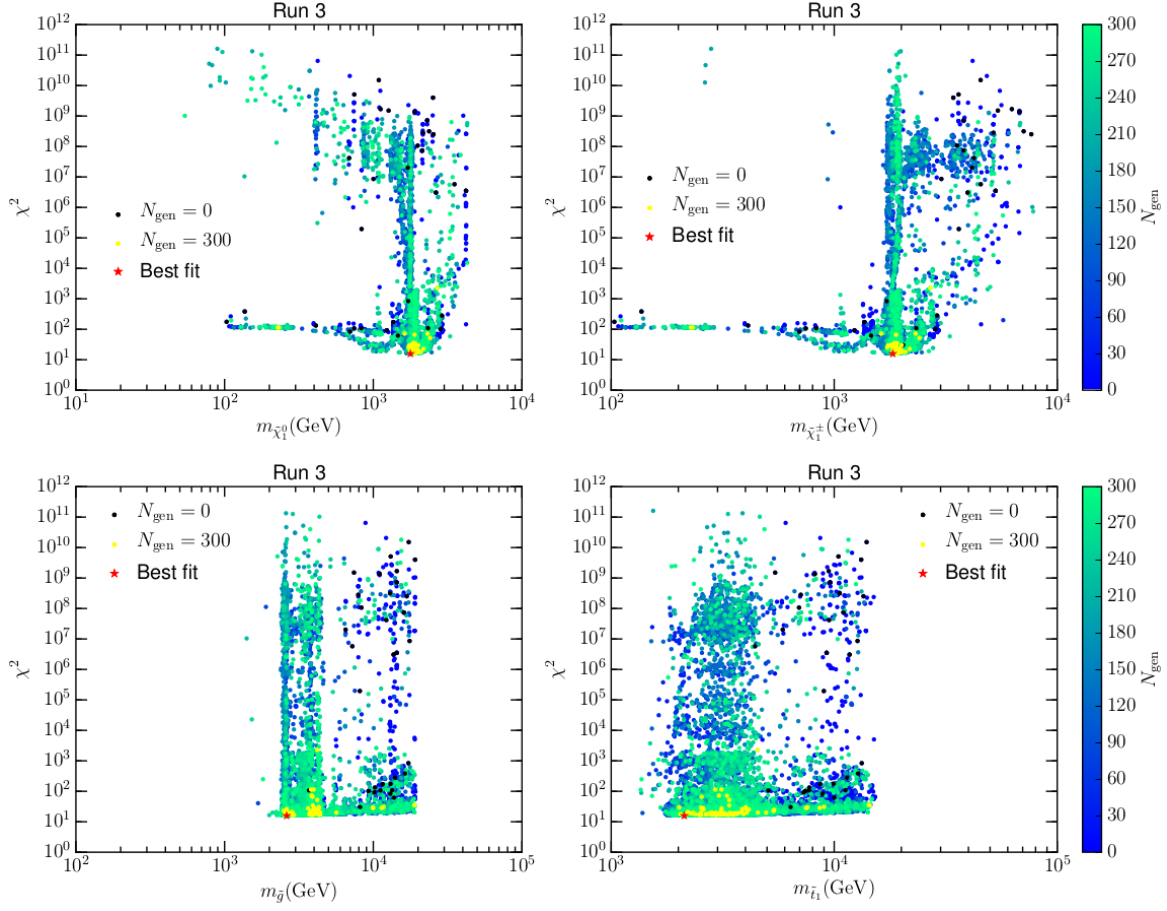
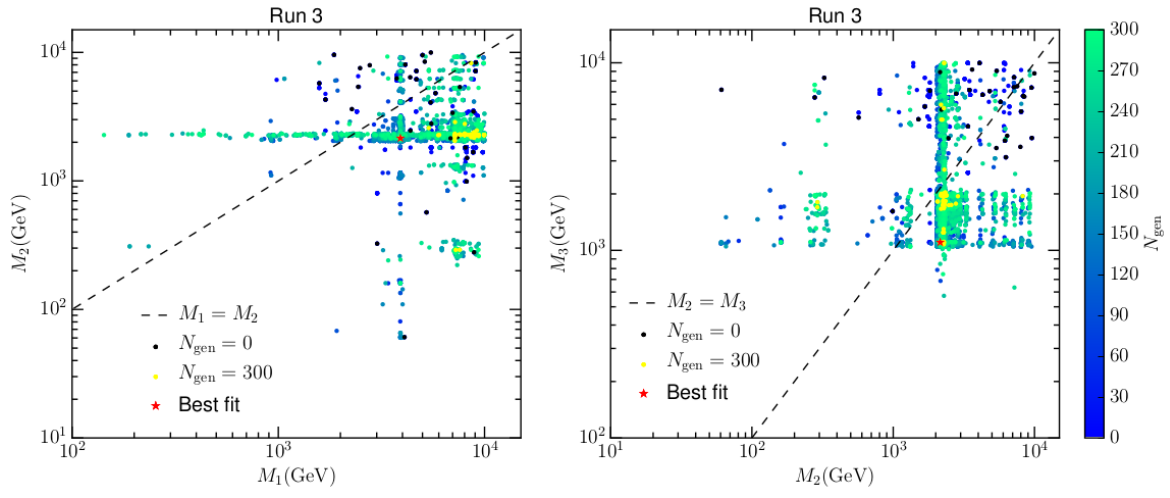


FIG. 11. Top left:  $\chi^2$  vs.  $BR(B_s^0 \rightarrow \mu^+ \mu^-)$ . Top right:  $\chi^2$  vs.  $BR(B \rightarrow X_s \gamma)$ . Bottom:  $\chi^2$  vs.  $\frac{BR(B_u \rightarrow \tau \nu)}{BR(B_u \rightarrow \tau \nu)_{\text{SM}}}$ . As a reference, we depict the mean value (solid black line) of each observable, and the  $1\sigma$  (grey) and  $2\sigma$  (light grey) regions around that value according to Table IV.



FIG. 14. Left:  $M_2$  vs.  $M_1$ . Right:  $M_3$  vs.  $M_2$



### B. The Galactic Centre excess

As a second example, let us consider fitting the observed GCE in the context of the pMSSM. In order to reproduce the measured gamma-ray spectrum, a small range of values for dark matter pair-annihilation cross section are required, around  $\langle\sigma v\rangle_0 \approx 10^{-26} \text{ cm}^3\text{s}^{-1}$ , which is roughly consistent with the expected value to obtain the correct relic abundance. Interestingly, this leads to an upper bound on  $\Omega_{\text{DM}}h^2$ , which in the previous example was not constrained from below. We can observe in Fig. 15 an increase of the global  $\chi^2$  for points where the neutralino relic density is too small. The requirement of fitting the GCE is consistent with recovering the correct relic abundance as well, which contributes to the clustering of solutions.

In Fig. 16 we can see how the GCE contributes to the total  $\chi^2$ . We can identify two types of behaviour. Points on the vertical branch correspond to those in which the annihilation cross section is too small and the neutralino relic abundance is too large, whereas points along the horizontal branch are those where the annihilation cross section is too large (thus the relic density is too small).

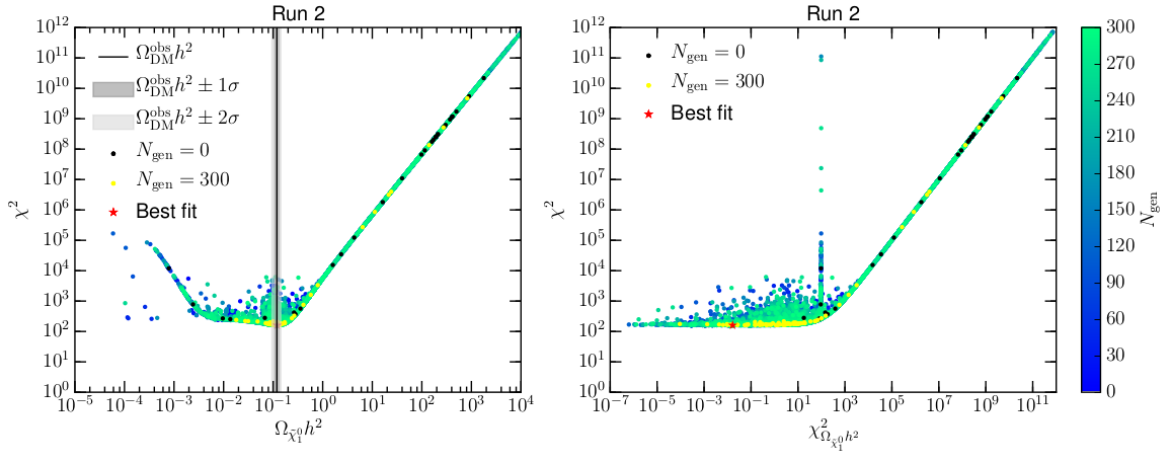


FIG. 15. Left:  $\chi^2$  vs.  $\Omega_{\tilde{\chi}_1^0} h^2$ . The solid black line corresponds to the  $\Omega_{\text{DM}} h^2$  mean value, see Table IV. As a reference, we show the  $1\sigma$  and  $2\sigma$  regions around that value in grey and light grey, respectively. Right:  $\chi^2$  vs.  $\chi^2_{\Omega_{\tilde{\chi}_1^0} h^2}$ . (Compare with Fig. 3)

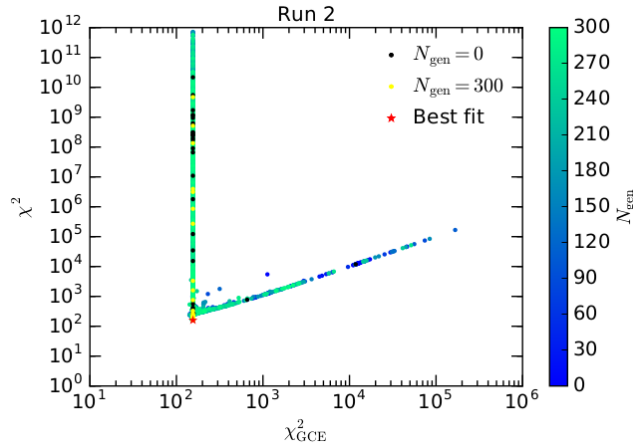


FIG. 16.  $\chi^2$  vs.  $\chi^2_{\text{GCE}}$ .

	Run 1	Run 2	Run 3	Run 4	Run 5
$\chi^2_{\Omega_{\tilde{\chi}_1^0} h^2}$	0.0040	0.0165	0.0015	0.0003	0.0472
$\chi^2_{\text{HiggsSignals}}$	1.2913	1.2812	1.2896	1.2938	1.2879
$\chi^2_{m_{h_0}}$	0.1411	0.1630	0.2316	0.5483	0.2214
$\chi^2_{M_W}$	0.2283	0.1652	0.3996	0.0999	0.2341
$\chi^2_{\sin^2 \theta_{\text{eff}}^{\text{lept}}}$	0.1509	0.1459	0.1266	0.1527	0.1416
$\chi^2_{\Gamma_Z}$	0.1208	0.0668	0.1584	0.0076	0.0425
$\chi^2_{\Gamma_Z^{\text{inv}}}$	2.3020	2.2954	2.2874	2.2985	2.2955
$\chi^2_{BR(B \rightarrow X_s \gamma)}$	0.1087	0.1283	0.1563	0.1016	0.0951
$\chi^2_{BR(B_s^0 \rightarrow \mu^+ \mu^-)}$	0.1575	0.1534	0.1508	0.1577	0.1547
$\chi^2_{\frac{BR(B_u \rightarrow \tau \nu)}{BR(B_u \rightarrow \tau \nu)_{\text{SM}}}}$	0.0140	0.0140	0.0142	0.0141	0.0140
$\chi^2_{\text{LEP}}$	0.0000	0.0000	0.0000	0.0000	0.0000
$\chi^2_{\text{LHC}}$	0.0000	0.0000	0.0000	0.0000	0.0000
$\chi^2_{\text{GCE}}$	155.3494	155.3459	155.3588	155.3656	155.3490
$\chi^2_{\text{tot}}$	159.8680	159.7755	160.1747	160.0401	159.8832

TABLE X. GCE: Contributions to the best fit  $\chi^2$ . In blue, we show the leading contribution, which comes from the fit to the Galactic Centre excess.

Observable	Run 1	Run 2	Run 3	Run 4	Run 5
$m_{h_0}$ (GeV)	124.33	124.28	124.12	123.60	124.14
$M_W$ (GeV)	80.376	80.378	80.374	80.379	80.376
$\sin^2 \theta_{\text{eff}}^{\text{lept}}$	0.23146	0.23146	0.23146	0.23146	0.23146
$\Gamma_Z$ (GeV)	2.4943	2.4946	2.4942	2.4950	2.4947
$\Gamma_Z^{\text{inv}}$ (GeV)	0.5017	0.5017	0.5017	0.5017	0.5017
$BR(B \rightarrow X_s \gamma) \times 10^4$	3.32	3.31	3.30	3.33	3.33
$BR(B_s^0 \rightarrow \mu^+ \mu^-) \times 10^9$	3.20	3.20	3.19	3.20	3.20
$\frac{BR(B_u \rightarrow \tau \nu)}{BR(B_u \rightarrow \tau \nu)_{\text{SM}}}$	1.00	1.00	1.00	1.00	1.00
$\Omega_{\tilde{\chi}_1^0} h^2$	0.1196	0.1203	0.1193	0.1186	0.1214
$m_{\tilde{\chi}_1^0}$ (TeV)	2.2366	2.2643	2.1660	2.1124	2.2386
$\langle \sigma v \rangle_0 \times 10^{26} (\text{cm}^3 \text{s}^{-1})$	2.11	2.06	2.24	2.35	2.10

TABLE XI. GCE: Best fit observables. In blue, we show the mass of the DM and  $\langle \sigma v \rangle_0$ .

The  $\chi^2$  for the best fit points is shown in Table X, together with the contribution for each individual observable. The total  $\chi^2 \approx 160$  is quite large in this example, but the main contribution is solely due to the fit to the GCE, whereas the rest of the observables are properly fit. It is illustrative to compare this table with Table V, which shows that the goodness of the fit to all observables is similar and that there is only one outlier (the fit to either  $\delta a_\mu^{\text{SUSY}}$  or the GCE). Likewise, the best fit to the different observables is shown in Table XI. We have included in this table the mass of the DM (the neutralino) and its annihilation cross section in the halo. We can observe that, although the annihilation cross section is of the right order of magnitude, the neutralino mass is approximately 2.2 TeV, too heavy compared to the best fit to the GCE, which requires DM masses of the order of 100 GeV or below, depending on the leading annihilation channel (see for example Ref. [67]). This is the main reason for the high value of  $\chi^2_{\text{GCE}}$ .

As a consequence, the input parameters for the best fit points, shown in Tab. XII, are indistinguishable from those obtained in the previous section, and the same holds for the low-energy supersymmetric spectrum of Tab. XIII. The spectrum for all the generations is shown in Fig. 17, in which the best fit points (red lines) seem to show more clustering than in the previous section (Fig. 2). Once more, the rest of the observables drive the evolution of the GA and we are left with a heavy SUSY spectrum, featuring wino-like 2.2 TeV neutralinos/charginos (see Fig. 18 for the neutralino composition), with a

heavy colour sector and where slepton masses vary in the range of 3 – 10 TeV. As we already observed in the previous section, the GA has singled out one observable (the GCE) which cannot be fit. As in the previous section, the Higgs mass is contributing to the GA evolution (see Fig. 19).

Parameter	Run 1	Run 2	Run 3	Run 4	Run 5
SM					
$[\alpha_{\text{EM}}(M_Z)^{\overline{MS}}]^{-1}$	128.0066	127.9962	127.9986	128.0143	127.9983
$\alpha_S(M_Z)^{\overline{MS}}$	0.1164	0.1170	0.1164	0.1177	0.1170
$m_b(\text{GeV})$	4.5603	4.6775	4.6551	4.6499	4.5627
$m_t(\text{GeV})$	175.3844	175.3538	175.18631	175.4313	175.3560
pMSSM (GUT scale)					
$M_1(\text{TeV})$	5.5273	9.1160	8.3262	9.0043	9.6308
$M_2(\text{TeV})$	2.6422	2.6594	2.5554	2.4849	2.6406
$M_3(\text{TeV})$	3.6930	3.2241	3.7310	1.8545	3.1646
$m_{H_u}(\text{TeV})$	2.7860	1.8275	4.5553	3.3882	0.7279
$m_{H_d}(\text{TeV})$	7.7773	6.7757	4.5548	7.7847	9.2033
$m_{\tilde{Q}_3}(\text{TeV})$	5.4058	5.6435	7.6979	4.1138	4.3414
$m_{\tilde{Q}_{1,2}}(\text{TeV})$	7.1555	8.8009	9.8729	6.1029	2.6357
$m_{\tilde{U}_3}(\text{TeV})$	0.2778	0.1488	1.2877	7.8291	2.4574
$m_{\tilde{U}_{1,2}}(\text{TeV})$	8.4336	2.7263	8.5276	8.9409	7.3785
$m_{\tilde{D}_3}(\text{TeV})$	3.0870	0.0584	3.1804	5.6241	3.7087
$m_{\tilde{D}_{1,2}}(\text{TeV})$	8.1973	5.1068	4.2454	3.3341	0.5251
$m_{\tilde{L}_3}(\text{TeV})$	8.6012	9.6593	9.7190	7.1871	9.7510
$m_{\tilde{L}_{1,2}}(\text{TeV})$	6.6443	7.0022	2.9389	7.9204	9.3869
$m_{\tilde{E}_3}(\text{TeV})$	2.6329	2.8818	3.6777	7.6730	2.6357
$m_{\tilde{E}_{1,2}}(\text{TeV})$	8.7945	7.9453	8.7390	4.1183	8.5795
$A_t(\text{TeV})$	-8.9734	-9.8566	-9.4894	-9.5476	-7.6226
$A_b(\text{TeV})$	-1.1680	4.7920	6.0644	1.1036	-0.3166
$A_\tau(\text{TeV})$	-7.1090	0.5658	0.4036	-1.1898	7.1546
$\tan \beta$	20.2322	19.3898	23.4440	23.2843	22.4006

TABLE XII. GCE: Best fit input parameters.

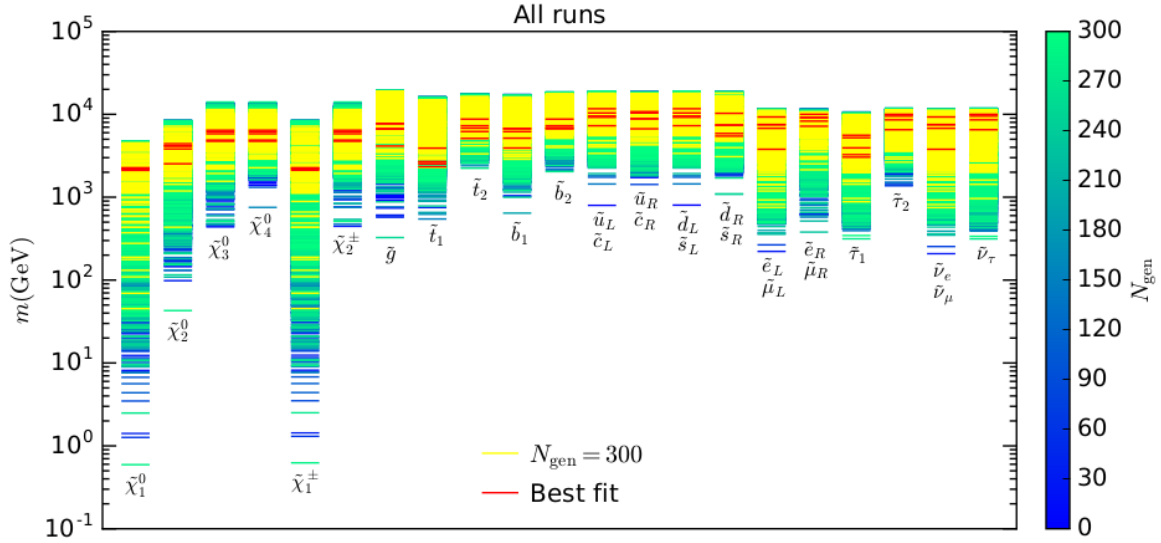


FIG. 17. SUSY spectrum for all the generations in the five runs. Yellow represents the results for the last generation and the red line corresponds to the best fit point. (Compare with Fig. 2)

m(TeV)	Run 1	Run 2	Run 3	Run 4	Run 5
$m_{\tilde{\chi}_1^0}$	2.2366	2.2643	2.1660	2.1124	2.2386
$m_{\tilde{\chi}_2^0}$	2.5307	4.1854	3.8210	4.1222	4.4207
$m_{\tilde{\chi}_3^0}$	5.8278	6.4265	6.1551	4.7343	4.8861
$m_{\tilde{\chi}_4^0}$	5.8285	6.4274	6.1560	4.7367	4.8893
$m_{\tilde{\chi}_1^\pm}$	2.2367	2.2645	2.1661	2.1126	2.2388
$m_{\tilde{\chi}_2^\pm}$	5.8289	6.4276	6.1562	4.7357	4.8876
$m_{\tilde{g}}$	7.6747	6.7363	7.7679	4.1441	6.6191
$m_{\tilde{t}_1}$	2.6531	2.6939	2.3329	3.9136	2.5218
$m_{\tilde{t}_2}$	7.2814	6.8084	8.7598	5.1231	6.1932
$m_{\tilde{b}_1}$	6.7616	5.1535	6.6804	3.9245	6.1878
$m_{\tilde{b}_2}$	7.2782	6.8041	8.7576	6.9004	6.6923
$m_{\tilde{u}_L}$	9.5393	10.3778	11.6758	7.2910	9.2023
$m_{\tilde{u}_R}$	10.3845	6.6924	10.7659	8.8563	8.8440
$m_{\tilde{d}_L}$	9.5395	10.3780	11.6759	7.2913	9.2025
$m_{\tilde{d}_R}$	10.2820	7.3770	7.4603	5.4592	5.8807
$m_{\tilde{c}_L}$	9.5392	10.3777	11.6757	7.2909	9.2022
$m_{\tilde{c}_R}$	10.3845	6.6923	10.7659	8.8563	8.8440
$m_{\tilde{s}_L}$	9.5394	10.3779	11.6759	7.2912	9.2024
$m_{\tilde{s}_R}$	10.2819	7.3768	7.4601	5.4590	5.8805
$m_{\tilde{\tau}_1}$	3.0421	3.2649	3.9357	5.5936	5.2167
$m_{\tilde{\tau}_2}$	8.5760	9.9785	9.9128	6.5254	9.5018
$m_{\tilde{e}_L}$	6.7806	7.5375	3.7867	7.4626	9.2988
$m_{\tilde{e}_R}$	9.1847	8.2899	9.0837	7.1857	10.0071
$m_{\tilde{\mu}_L}$	6.7801	7.5371	3.7860	7.4621	9.2982
$m_{\tilde{\mu}_R}$	9.1839	8.2892	9.0831	7.1847	10.0060
$m_{\tilde{\nu}_e}$	6.7798	7.5367	3.7856	7.4619	9.2982
$m_{\tilde{\nu}_\mu}$	6.7793	7.5364	3.7848	7.4614	9.2975
$m_{\tilde{\nu}_\tau}$	8.5753	9.9779	9.9122	6.5243	9.5011
$m_{H^0}$	9.4674	9.5080	7.5931	8.3477	9.9123
$m_{A^0}$	9.4671	9.5074	7.5931	8.3477	9.9121
$m_{H^\pm}$	9.4675	9.5079	7.5935	8.3482	9.9126

TABLE XIII. GCE: Best fit SUSY spectrum.

Finally, Fig. 20 shows the predictions for direct and indirect dark matter detection. The results for direct detection are very similar to those of the previous section (Fig. 5), with neutralinos marginally within the sensitivity of future multi-ton xenon and argon experiments. The plot of the annihilation cross-section in Fig. 20 still shows the best fit point with heavy neutralinos and  $\langle\sigma v\rangle_0 \approx 10^{-26} \text{ cm}^3\text{s}^{-1}$ . As mentioned above, this is far from the preferred region that would explain the GCE in terms of DM with masses of order 100 GeV.

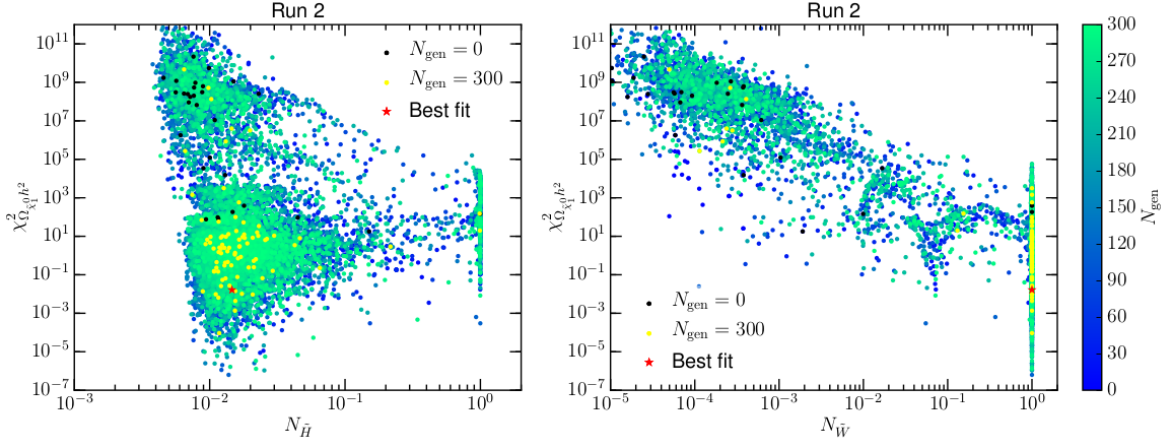


FIG. 18.  $\chi^2_{\Omega_{\tilde{\chi}_1^0} h^2}$  vs. the Higgsino (left) and wino (right) component of the lightest neutralino. (Compare with Fig. 4)

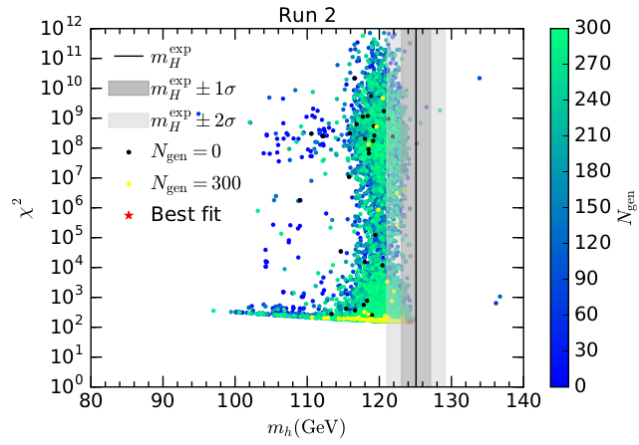


FIG. 19.  $\chi^2$  vs. Higgs mass. (Compare with Fig. 6)

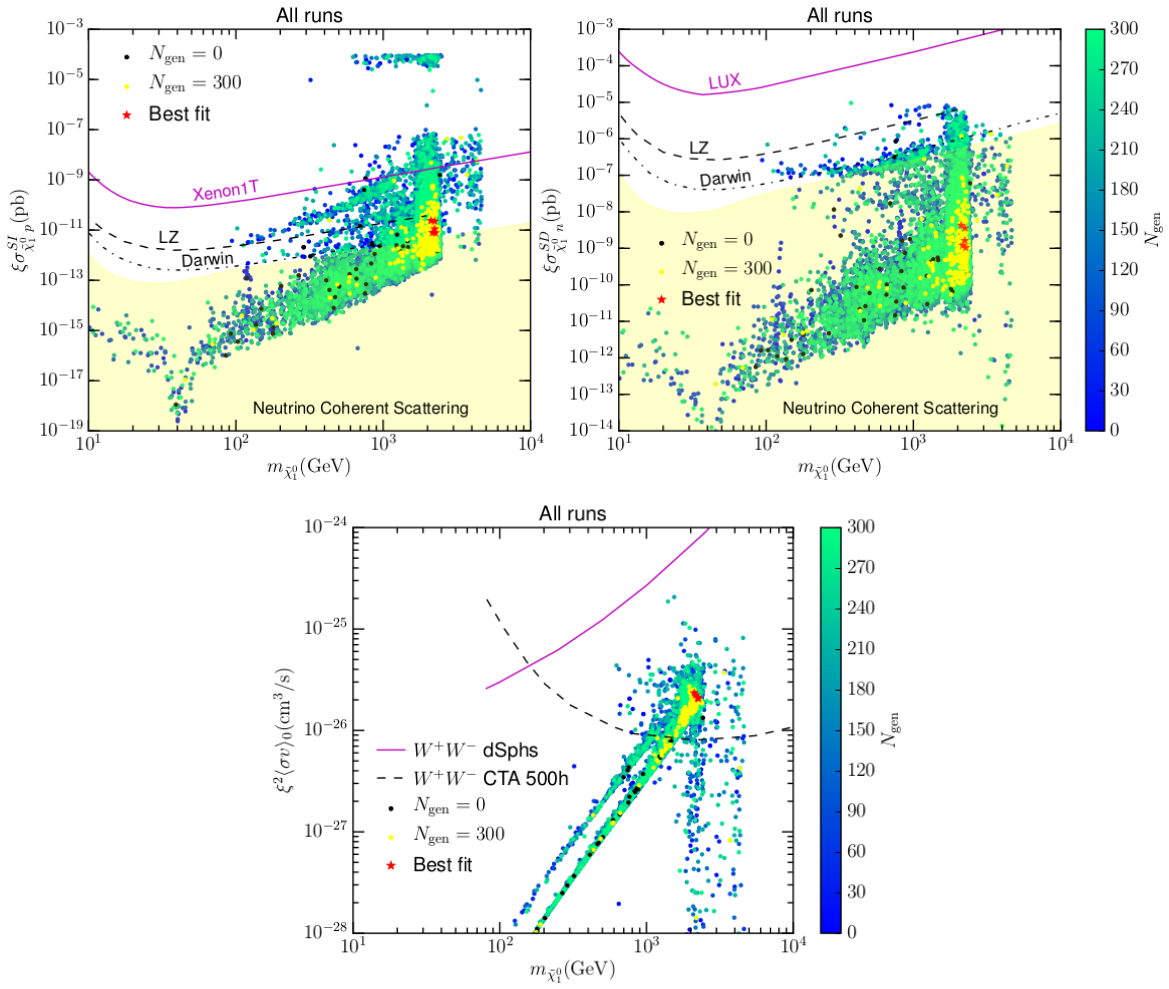


FIG. 20. Top left: Theoretical predictions for  $\xi\sigma_{\tilde{\chi}_1^0 p}^{SI}$  as a function of  $m_{\tilde{\chi}_1^0}$  for all the runs. Top right: Predictions for  $\xi\sigma_{\tilde{\chi}_1^0 n}^{SD}$  vs.  $m_{\tilde{\chi}_1^0}$ . Bottom: Thermally averaged neutralino annihilation cross section in the Galactic halo,  $\xi^2\langle\sigma v\rangle_0$ , as a function of the lightest neutralino mass. The colour code and lines are as in Fig. 5.

## V. CONCLUSIONS

In this article, we have investigated the use of Genetic Algorithms (GAs) to study the cross-compatibility of experimental constraints in high-dimensional models. We have focused on the pMSSM, which features 19 input parameters (soft supersymmetry-breaking terms) defined at the GUT scale, and 4 nuisance parameters (the electromagnetic coupling constant evaluated at the Z-boson pole mass, the strong coupling constant at  $M_Z$ , the pole mass of the top quark, and the pole mass of the bottom quark), for a total of 23 parameters.

GAs seem to be extremely effective in finding a best fit point that minimises the total  $\chi^2$ . With only  $10^4$  model evaluations, solutions could be found that were consistent with results that employ MCMC scans to probe the whole parameter space, and that require many more model evaluations. The GA leads to a final population of models with a roughly 2 TeV wino-like neutralino, which has the correct relic abundance due to coannihilations with a quasi-degenerate chargino. The resulting SUSY spectrum is shown in Fig. 2 (Table VIII) and Fig. 17 (Table XIII). The coloured sector is predicted to be heavy,  $m_{\tilde{g}} > 5 \text{ TeV}$ , except for the lightest stop, for which  $m_{\tilde{t}_1} \approx 2.3 \text{ TeV}$ . We find that the pMSSM does not give a clear prediction for the slepton sector, and the masses span a wide range,  $m_{\tilde{\tau}_1} \sim 2.3 - 8 \text{ TeV}$ . The neutralino relic abundance and the Higgs mass are the most important constraints driving the GA evolution.

We also demonstrated how one can deal with potential signals for new physics, by considering the muon anomalous magnetic moment (which shows a large deviation with respect to the SM value) and the Fermi-LAT excess in the gamma ray spectrum from the Galactic Centre (which can be interpreted as a hint for DM pair-annihilation). A GA proves to be an excellent tool for assessing the compatibility of these observations with all the other experimental constraints, including LHC and LEP bounds on SUSY masses and on the Higgs sector, Planck measurement of the DM relic abundance, and constraints on low-energy observables. Moreover, it also yields a good diagnosis of which are the problematic observables. In both these examples, the main contribution to the final  $\chi^2$  was due to either the muon anomalous magnetic moment,  $\chi_{\delta a_\mu}^2 \approx 12$ , or the Galactic Centre excess,  $\chi_{\text{GCE}}^2 \approx 155$ , whereas the fit to all the other observables was good. This is an indication that the pMSSM, despite its large number of free parameters, cannot successfully include these potential hints for new physics. (A compromise could in principle have been possible, in which they were fit reasonably well by sacrificing  $\chi^2$  elsewhere, but this turned out to be impossible.)

In our view, GAs offer a superior approach to probing BSM physics, especially in an era when the underlying principles are less clear, but when there are nevertheless definite hints of new physics. The technique we discussed here could for example be easily applied to the most general form of MSSM with its 124 parameters, as well as more general Higgs sectors, with no obvious impediment. Compared to other more conventional techniques, GAs are able (by sacrificing a little statistical rigour) to divine patterns of interesting models, and assess their consistency exceedingly quickly.

## Acknowledgements

We thank G. Gómez-Vargas, D. V. Malyshev and M.A. Sánchez Conde. SR was partially supported by MINECO, Spain, under contract FPA2016-78022-P, Centro de excelencia Severo Ochoa Program under grant SEV-2014-0398, the Campus of Excellence UAM+CSIC and the Australian Research Council.



### Appendix A: Additional plots

In this appendix, we include some extra figures that show the GA evolution of some of the 19 input parameters of the pMSSM for the example discussed in Section IVA, where we attempt to fit the muon anomalous magnetic moment. As in the other plots of this paper, these figures should not be understood as “scatter plots” or general explorations of the parameter space, but rather as an indication of the genome evolution over different generations. In Figures 22-27, we compare the results for runs 1, 2, 3, and 7 showing how different runs lead to compatible results. We have not included plots corresponding to Section IVB, as they look very similar.

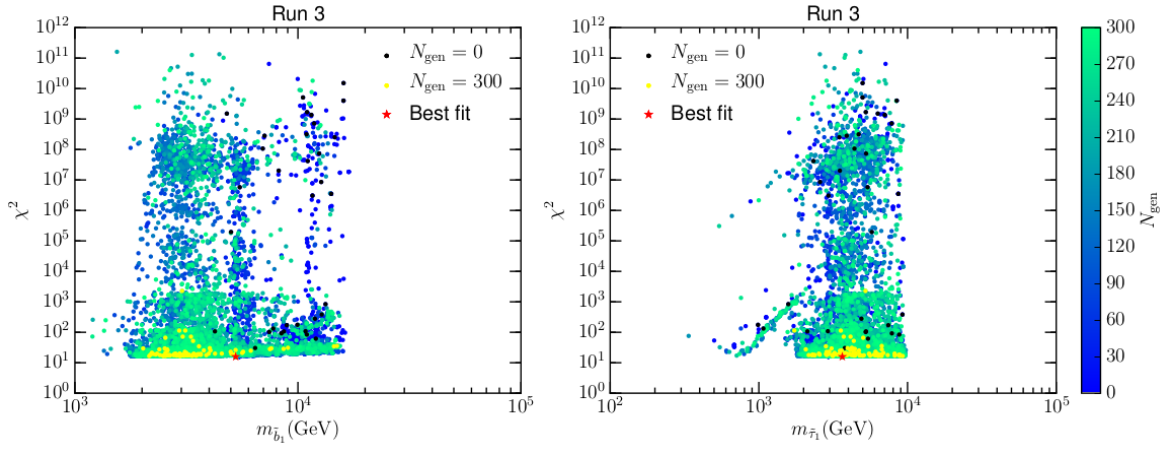


FIG. 21. Left:  $\chi^2$  vs.  $m_{\tilde{b}_1}$ . Right:  $\chi^2$  vs.  $m_{\tilde{\tau}_1}$ . The colour map represents the generation number from 0 to 300. The initial guesses (generation 0) are depicted in black and the final generation in yellow. The red star corresponds to the best fit.

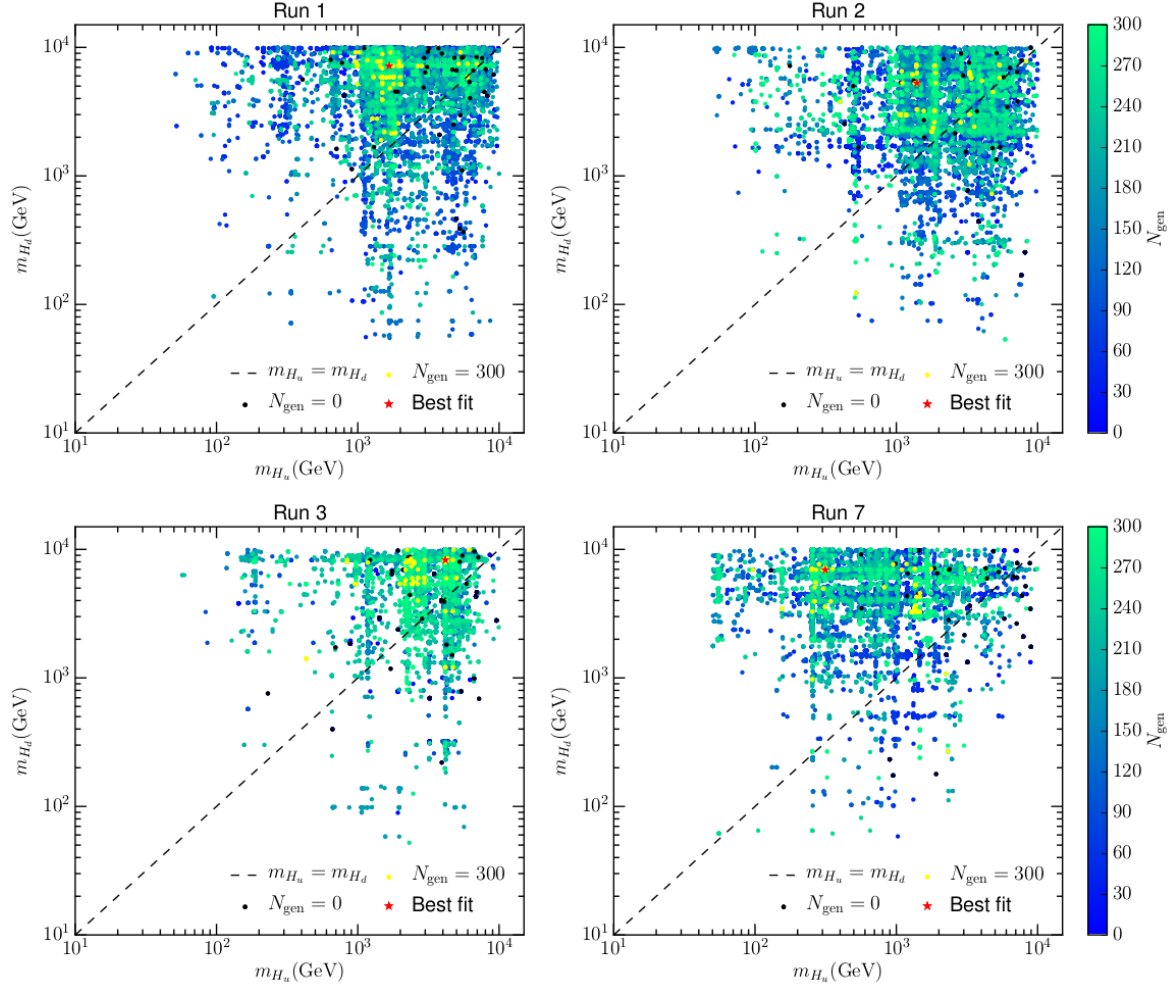


FIG. 22.  $m_{H_d}$  vs.  $m_{H_u}$ , top left (run 1), top right (run 2), bottom left (run 3), bottom right (run 7).

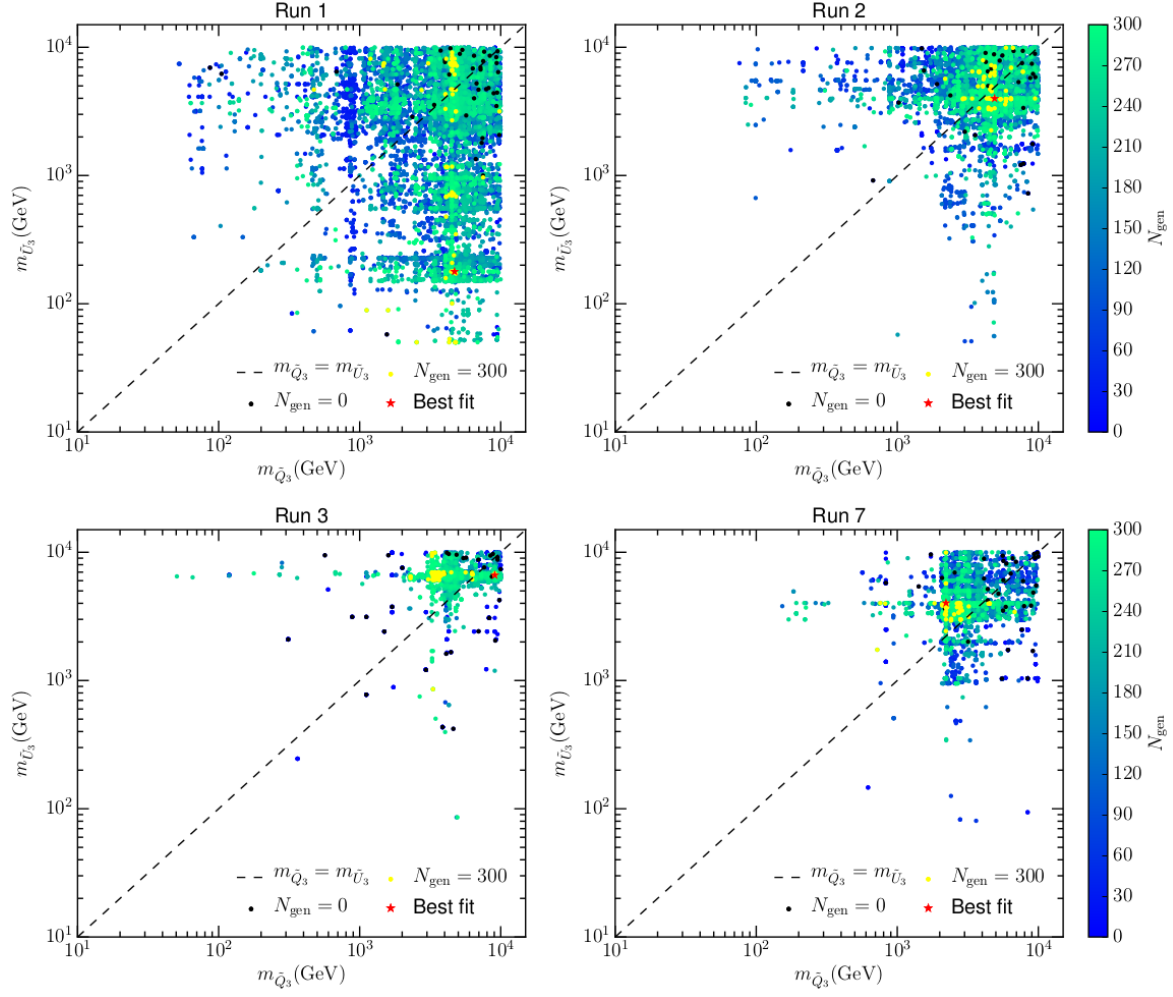


FIG. 23.  $m_{\tilde{U}_3}$  vs.  $m_{\tilde{Q}_3}$ , top left (run 1), top right (run 2), bottom left (run 3), bottom right (run 7).

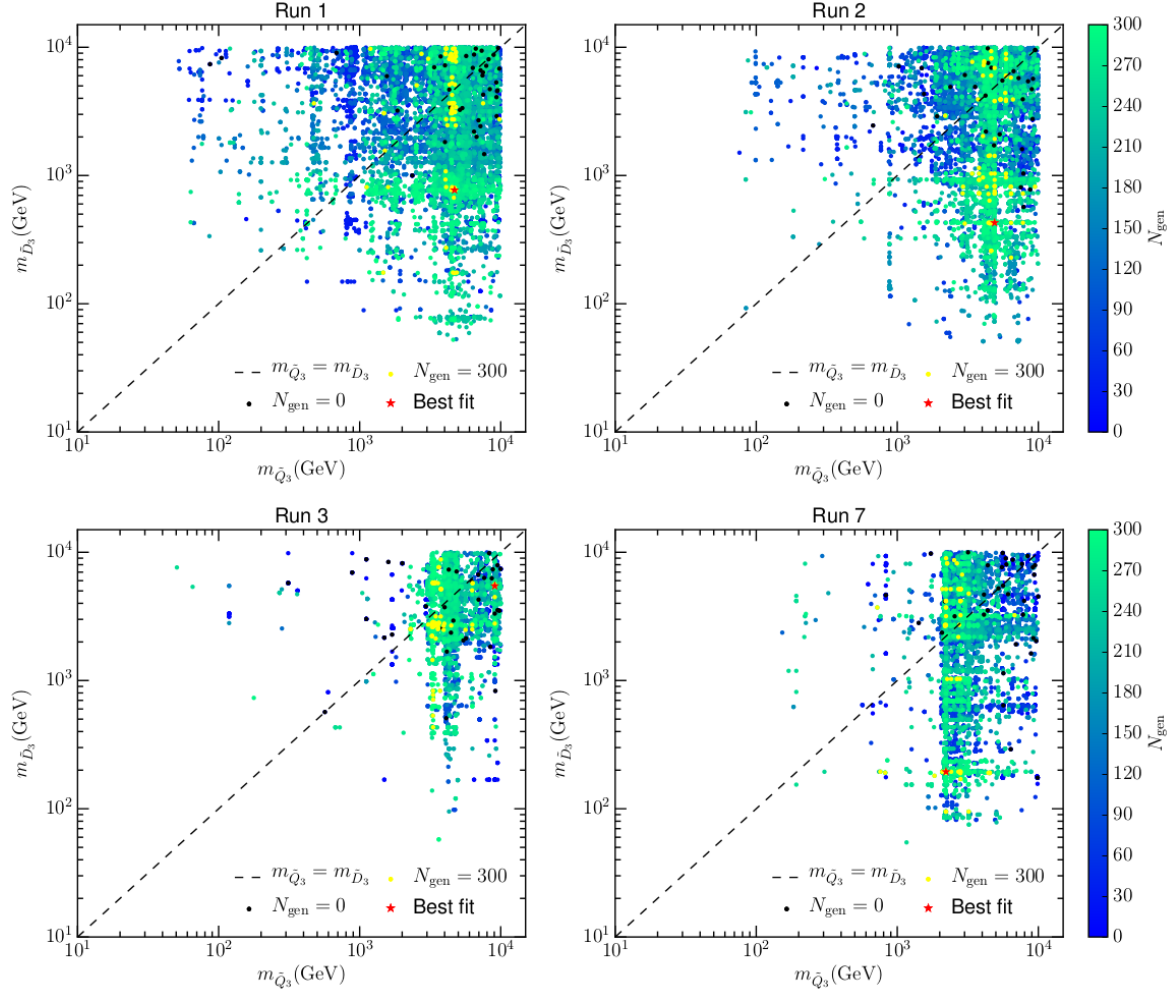


FIG. 24.  $m_{\tilde{D}_3}$  vs.  $m_{\tilde{Q}_3}$ , top left (run 1), top right (run 2), bottom left (run 3), bottom right (run 7).

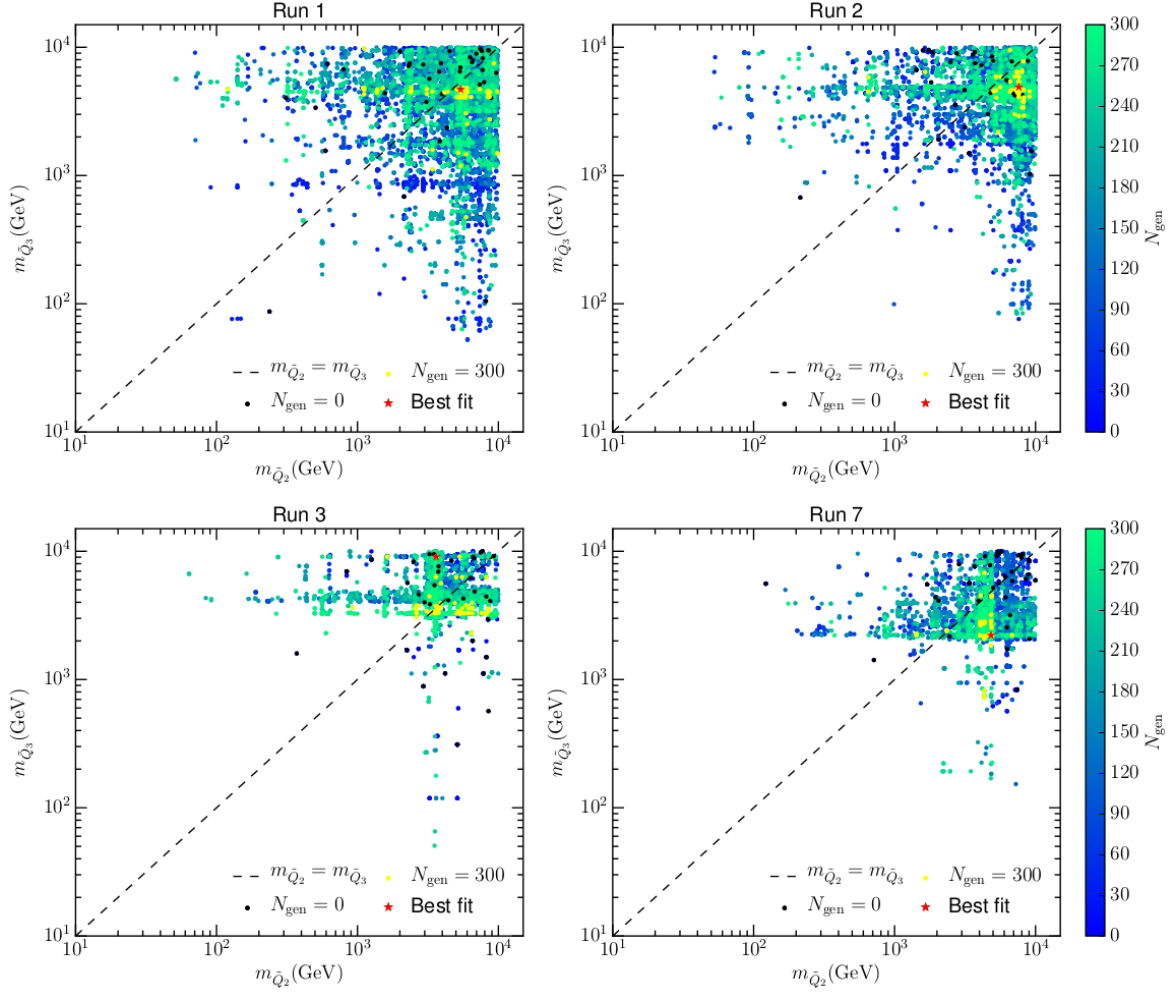


FIG. 25.  $m_{\tilde{Q}_3}$  vs.  $m_{\tilde{Q}_2}$ , top left (run 1), top right (run 2), bottom left (run 3), bottom right (run 7).

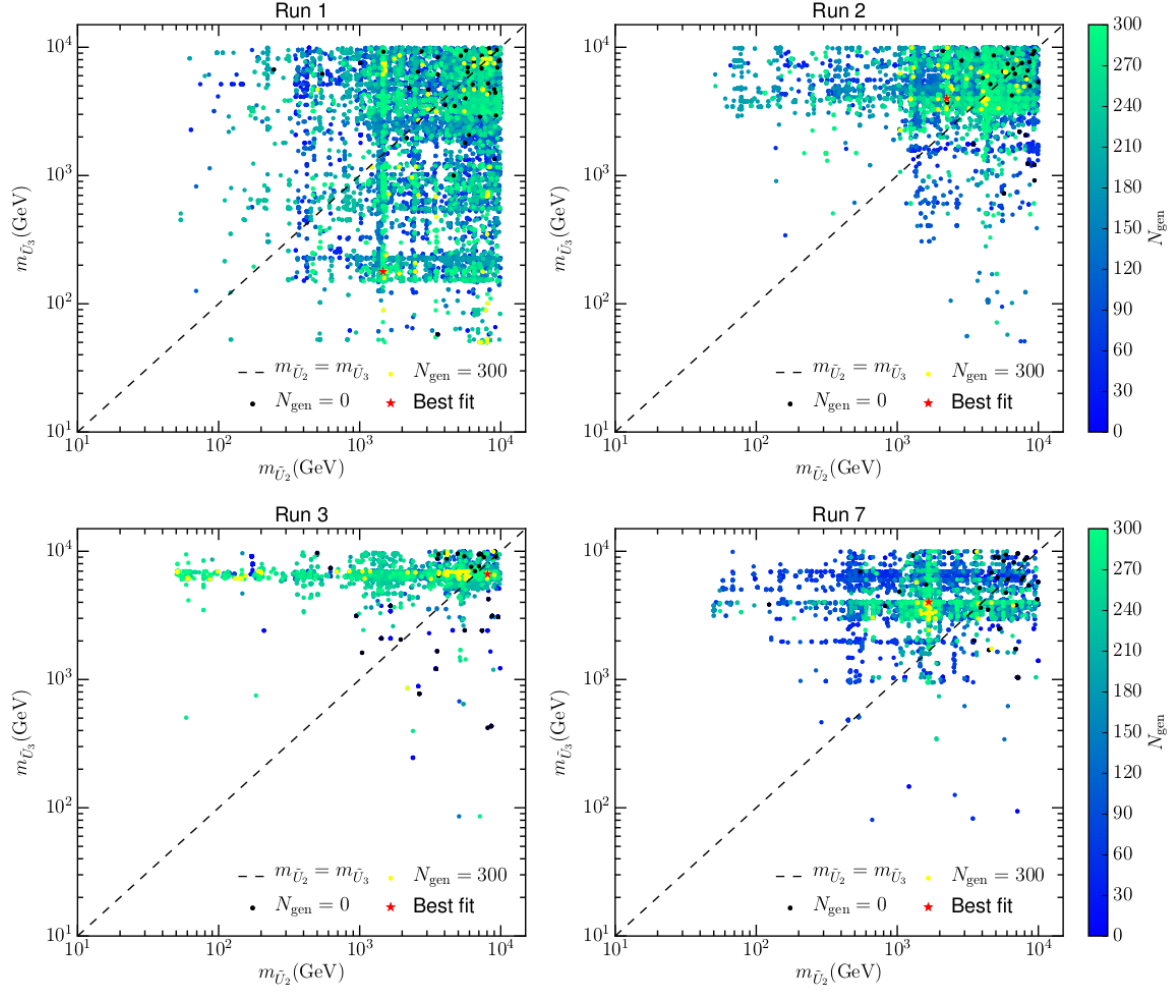


FIG. 26.  $m_{\tilde{U}_3}$  vs.  $m_{\tilde{U}_2}$ , top left (run 1), top right (run 2), bottom left (run 3), bottom right (run 7).

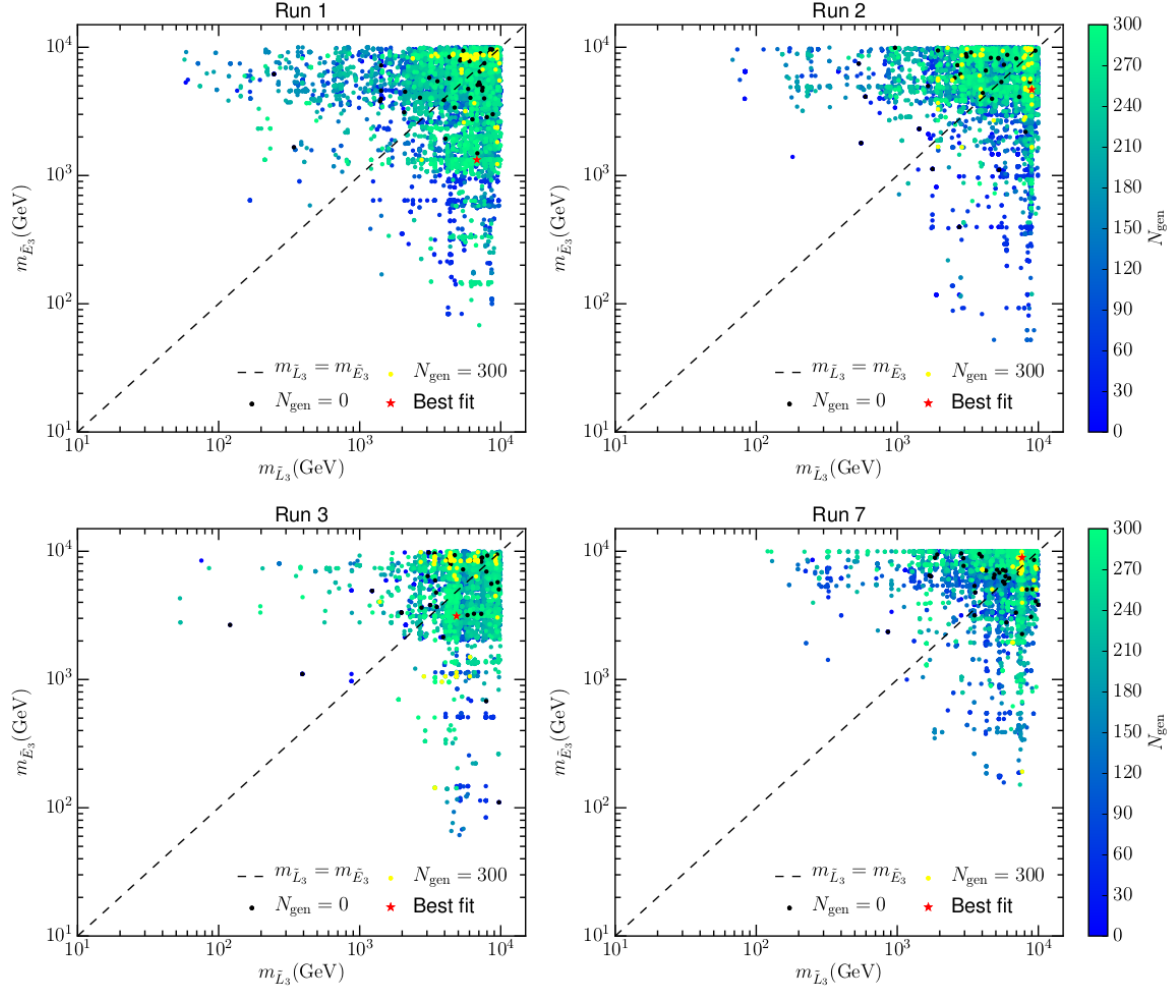


FIG. 27.  $m_{\tilde{E}_3}$  vs.  $m_{\tilde{L}_3}$ , top left (run 1), top right (run 2), bottom left (run 3), bottom right (run 7).



- 
- [1] MSSM WORKING GROUP collaboration, A. Djouadi et al., *The Minimal supersymmetric standard model: Group summary report*, in *GDR (Groupement De Recherche) - Supersymetrie Montpellier, France, April 15-17, 1998*, 1998. [hep-ph/9901246](#).
  - [2] C. F. Berger, J. S. Gainer, J. L. Hewett and T. G. Rizzo, *Supersymmetry Without Prejudice*, *JHEP* **02** (2009) 023, [[0812.0980](#)].
  - [3] S. S. AbdusSalam, B. C. Allanach, F. Quevedo, F. Feroz and M. Hobson, *Fitting the Phenomenological MSSM*, *Phys. Rev.* **D81** (2010) 095012, [[0904.2548](#)].
  - [4] M. Cahill-Rowley, J. L. Hewett, A. Ismail and T. G. Rizzo, *pMSSM Studies at the 7, 8 and 14 TeV LHC*, in *Proceedings, 2013 Community Summer Study on the Future of U.S. Particle Physics: Snowmass on the Mississippi (CSS2013): Minneapolis, MN, USA, July 29-August 6, 2013*, 2013. [1307.8444](#).
  - [5] M. Cahill-Rowley, J. L. Hewett, A. Ismail and T. G. Rizzo, *Lessons and prospects from the pMSSM after LHC Run I*, *Phys. Rev.* **D91** (2015) 055002, [[1407.4130](#)].
  - [6] J. Holland, *Adaptation in Natural and Artificial Systems*. The MIT Press reprinted, 1992.
  - [7] E. David, *Genetic Algorithms in Search, Optimization and Machine Learning*. Addison-Wesley, 1989.
  - [8] J. Holland, *The Royal Road for Genetic Algorithms: Fitness Landscapes and GA Performance*, in *Toward a Practice of Autonomous Systems: proceedings of the first European conference on Artificial Life* (F. J. Varela and P. Bourguine, eds.), MIT Press, 1992.
  - [9] C. Reeves and J. Rowe, *Genetic Algorithms: Principles and Perspectives*. Springer, 2002.
  - [10] R. Haupt and S. Haupt, *Practical genetic algorithms*. Wiley, 2nd ed., 2004.
  - [11] D. Michalewicz, *How to Solve It: Modern Heuristics*. Springer. Z Fogel 2nd ed., 2004.
  - [12] F. Feroz and M. P. Hobson, *Multimodal nested sampling: an efficient and robust alternative to MCMC methods for astronomical data analysis*, *Mon. Not. Roy. Astron. Soc.* **384** (2008) 449, [[0704.3704](#)].
  - [13] F. Feroz, M. P. Hobson and M. Bridges, *MultiNest: an efficient and robust Bayesian inference tool for cosmology and particle physics*, *Mon. Not. Roy. Astron. Soc.* **398** (2009) 1601–1614, [[0809.3437](#)].
  - [14] F. Feroz, M. P. Hobson, E. Cameron and A. N. Pettitt, *Importance Nested Sampling and the MultiNest Algorithm*, [1306.2144](#).
  - [15] T. Jones and S. Forrest, *Fitness distance correlation as a measure of problem difficulty for genetic algorithms*, in *Proceedings of the 6th International Conference on Genetic Algorithms* (L. J. Eshelman, ed.), 1995.
  - [16] P. Collard, A. Gaspar, M. Clergue and C. Escazu, *Fitness Distance Correlation, as statistical measure of Genetic Algorithm difficulty, revisited*. 1998.
  - [17] J. Blåbäck, U. Danielsson and G. Dibitetto, *Fully stable dS vacua from generalised fluxes*, *JHEP* **08** (2013) 054, [[1301.7073](#)].
  - [18] S. Abel and J. Rizos, *Genetic Algorithms and the Search for Viable String Vacua*, *JHEP* **08** (2014) 010, [[1404.7359](#)].
  - [19] A. Yamaguchi and H. Nakajima, *Landau gauge fixing supported by genetic algorithm*, *Nucl. Phys. Proc. Suppl.* **83** (2000) 840–842, [[hep-lat/9909064](#)].
  - [20] B. C. Allanach, D. Grellscheid and F. Quevedo, *Genetic algorithms and experimental discrimination of SUSY models*, *JHEP* **07** (2004) 069, [[hep-ph/0406277](#)].
  - [21] Y. Akrami, P. Scott, J. Edsjo, J. Conrad and L. Bergstrom, *A Profile Likelihood Analysis of the Constrained MSSM with Genetic Algorithms*, *JHEP* **04** (2010) 057, [[0910.3950](#)].
  - [22] P. Charbonneau, *Genetic Algorithms in Astronomy and Astrophysics*, *ApJS* **101** (Dec., 1995) 309.
  - [23] P. Charbonneau, *A User's guide to PIKAIA 1.0*, Tech. Rep. TN-418+IA, National Center for Atmospheric Research, Dec., 1995.
  - [24] P. Charbonneau, *An introduction to genetic algorithms for numerical optimization*, Tech. Rep. TN-450+IA, National Center for Atmospheric Research, Mar., 2002.
  - [25] P. Charbonneau, *Release Notes for PIKAIA 1.2*, Tech. Rep. TN-451+STR, National Center for Atmospheric Research, Mar., 2002.
  - [26] PARTICLE DATA GROUP collaboration, C. Patrignani et al., *Review of Particle Physics*, *Chin. Phys.* **C40** (2016) 100001.
  - [27] B. C. Allanach, *SOFTSUSY: a program for calculating supersymmetric spectra*, *Comput. Phys. Commun.* **143** (2002) 305–331, [[hep-ph/0104145](#)].
  - [28] S. Heinemeyer, W. Hollik and G. Weiglein, *FeynHiggs: A Program for the calculation of the masses of the neutral CP even Higgs bosons in the MSSM*, *Comput. Phys. Commun.* **124** (2000) 76–89, [[hep-ph/9812320](#)].
  - [29] S. Heinemeyer, W. Hollik and G. Weiglein, *The Masses of the neutral CP - even Higgs bosons in the MSSM: Accurate analysis at the two loop level*, *Eur. Phys. J.* **C9** (1999) 343–366, [[hep-ph/9812472](#)].

- [30] T. Hahn, S. Heinemeyer, W. Hollik, H. Rzehak and G. Weiglein, *High-Precision Predictions for the Light CP -Even Higgs Boson Mass of the Minimal Supersymmetric Standard Model*, *Phys. Rev. Lett.* **112** (2014) 141801, [[1312.4937](#)].
- [31] H. Bahl and W. Hollik, *Precise prediction for the light MSSM Higgs boson mass combining effective field theory and fixed-order calculations*, *Eur. Phys. J.* **C76** (2016) 499, [[1608.01880](#)].
- [32] D. Yu. Bardin, P. Christova, M. Jack, L. Kalinovskaya, A. Olchevski, S. Riemann et al., *ZFITTER v.6.21: A Semianalytical program for fermion pair production in  $e^+e^-$  annihilation*, *Comput. Phys. Commun.* **133** (2001) 229–395, [[hep-ph/9908433](#)].
- [33] A. B. Arbuzov, M. Awramik, M. Czakon, A. Freitas, M. W. Grunewald, K. Monig et al., *ZFITTER: A Semi-analytical program for fermion pair production in  $e^+e^-$  annihilation, from version 6.21 to version 6.42*, *Comput. Phys. Commun.* **174** (2006) 728–758, [[hep-ph/0507146](#)].
- [34] G. Belanger, F. Boudjema, A. Pukhov and A. Semenov, *MicrOMEGAs: A Program for calculating the relic density in the MSSM*, *Comput. Phys. Commun.* **149** (2002) 103–120, [[hep-ph/0112278](#)].
- [35] P. Bechtle, O. Brein, S. Heinemeyer, G. Weiglein and K. E. Williams, *HiggsBounds: Confronting Arbitrary Higgs Sectors with Exclusion Bounds from LEP and the Tevatron*, *Comput. Phys. Commun.* **181** (2010) 138–167, [[0811.4169](#)].
- [36] P. Bechtle, O. Brein, S. Heinemeyer, O. Stål, T. Stefaniak, G. Weiglein et al., *HiggsBounds – 4: Improved Tests of Extended Higgs Sectors against Exclusion Bounds from LEP, the Tevatron and the LHC*, *Eur. Phys. J.* **C74** (2014) 2693, [[1311.0055](#)].
- [37] P. Bechtle, S. Heinemeyer, O. Stål, T. Stefaniak and G. Weiglein, *HiggsSignals: Confronting arbitrary Higgs sectors with measurements at the Tevatron and the LHC*, *Eur. Phys. J.* **C74** (2014) 2711, [[1305.1933](#)].
- [38] D. Barducci, G. Belanger, J. Bernon, F. Boudjema, J. Da Silva, S. Kraml et al., *Collider limits on new physics within micrOMEGAs 4.3*, *Comput. Phys. Commun.* **222** (2018) 327–338, [[1606.03834](#)].
- [39] R. Ruiz de Austri, R. Trotta and L. Roszkowski, *A Markov chain Monte Carlo analysis of the CMSSM*, *JHEP* **05** (2006) 002, [[hep-ph/0602028](#)].
- [40] F. Ambrogì, S. Kraml, S. Kulkarni, U. Laa, A. Lessa, V. Magerl et al., *SModelS v1.1 user manual*, [1701.06586](#).
- [41] S. Kraml, S. Kulkarni, U. Laa, A. Lessa, W. Magerl, D. Proschofsky et al., *SModelS: a tool for interpreting simplified-model results from the LHC and its application to supersymmetry*, *Eur. Phys. J.* **C74** (2014) 2868, [[1312.4175](#)].
- [42] B. C. Allanach, A. Bednyakov and R. Ruiz de Austri, *Higher order corrections and unification in the minimal supersymmetric standard model: SOFTSUSY3.5*, *Comput. Phys. Commun.* **189** (2015) 192–206, [[1407.6130](#)].
- [43] B. C. Allanach and T. Cridge, *The Calculation of Sparticle and Higgs Decays in the Minimal and Next-to-Minimal Supersymmetric Standard Models: SOFTSUSY4.0*, *Comput. Phys. Commun.* **220** (2017) 417–502, [[1703.09717](#)].
- [44] T. Sjöstrand, S. Mrenna and P. Z. Skands, *PYTHIA 6.4 Physics and Manual*, *JHEP* **0605** (2006) 026, [[hep-ph/0603175](#)].
- [45] T. Sjöstrand, S. Ask, J. R. Christiansen, R. Corke, N. Desai, P. Ilten et al., *An Introduction to PYTHIA 8.2*, *Comput. Phys. Commun.* **191** (2015) 159–177, [[1410.3012](#)].
- [46] W. Beenakker, R. Hopker, M. Spira and P. Zerwas, *Squark and gluino production at hadron colliders*, *Nucl. Phys.* **B492** (1997) 51–103, [[hep-ph/9610490](#)].
- [47] W. Beenakker, M. Kramer, T. Plehn, M. Spira and P. Zerwas, *Stop production at hadron colliders*, *Nucl. Phys.* **B515** (1998) 3–14, [[hep-ph/9710451](#)].
- [48] A. Kulesza and L. Motyka, *Threshold resummation for squark-antisquark and gluino-pair production at the LHC*, *Phys. Rev. Lett.* **102** (2009) 111802, [[0807.2405](#)].
- [49] A. Kulesza and L. Motyka, *Soft gluon resummation for the production of gluino-gluino and squark-antisquark pairs at the LHC*, *Phys. Rev.* **D80** (2009) 095004, [[0905.4749](#)].
- [50] W. Beenakker, S. Brensing, M. Kramer, A. Kulesza, E. Laenen et al., *Soft-gluon resummation for squark and gluino hadroproduction*, *JHEP* **0912** (2009) 041, [[0909.4418](#)].
- [51] W. Beenakker, S. Brensing, M. Kramer, A. Kulesza, E. Laenen et al., *Supersymmetric top and bottom squark production at hadron colliders*, *JHEP* **1008** (2010) 098, [[1006.4771](#)].
- [52] W. Beenakker, S. Brensing, M. Kramer, A. Kulesza, E. Laenen et al., *Squark and Gluino Hadroproduction*, *Int. J. Mod. Phys.* **A26** (2011) 2637–2664, [[1105.1110](#)].
- [53] M. Papucci, K. Sakurai, A. Weiler and L. Zeune, *Fastlim: a fast LHC limit calculator*, *Eur. Phys. J.* **C74** (2014) 3163, [[1402.0492](#)].
- [54] SLD ELECTROWEAK GROUP, DELPHI, ALEPH, SLD, SLD HEAVY FLAVOUR GROUP, OPAL, LEP ELECTROWEAK WORKING GROUP, L3 collaboration, S. Schael et al., *Precision electroweak measurements on the Z resonance*, *Phys. Rept.* **427** (2006) 257–454, [[hep-ex/0509008](#)].

- [55] DELPHI, OPAL, LEP ELECTROWEAK, ALEPH, L3 collaboration, S. Schael et al., *Electroweak Measurements in Electron-Positron Collisions at W-Boson-Pair Energies at LEP*, *Phys. Rept.* **532** (2013) 119–244, [[1302.3415](#)].
- [56] ATLAS, CMS collaboration, G. Aad et al., *Combined Measurement of the Higgs Boson Mass in pp Collisions at  $\sqrt{s} = 7$  and 8 TeV with the ATLAS and CMS Experiments*, *Phys. Rev. Lett.* **114** (2015) 191803, [[1503.07589](#)].
- [57] HEAVY FLAVOR AVERAGING GROUP (HFAG) collaboration, Y. Amhis et al., *Averages of b-hadron, c-hadron, and  $\tau$ -lepton properties as of summer 2014*, **1412.7515**.
- [58] LHCb, CMS collaboration, V. Khachatryan et al., *Observation of the rare  $B_s^0 \rightarrow \mu^+ \mu^-$  decay from the combined analysis of CMS and LHCb data*, *Nature* **522** (2015) 68–72, [[1411.4413](#)].
- [59] A. G. Akeroyd and F. Mahmoudi, *Measuring  $V_{ub}$  and probing SUSY with double ratios of purely leptonic decays of B and D mesons*, *JHEP* **10** (2010) 038, [[1007.2757](#)].
- [60] PLANCK collaboration, P. A. R. Ade et al., *Planck 2015 results. XIII. Cosmological parameters*, *Astron. Astrophys.* **594** (2016) A13, [[1502.01589](#)].
- [61] ALEPH collaboration, A. Heister et al., *Absolute mass lower limit for the lightest neutralino of the MSSM from  $e^+ e^-$  data at  $s^{**}(1/2)$  up to 209-GeV*, *Phys. Lett.* **B583** (2004) 247–263.
- [62] ALEPH, DELPHI, L3 AND OPAL collaboration, *Combined LEP Selectron/Smuon/Stau Results, 183-208 GeV*, Tech. Rep. note LEPSUSYWG/04-01.1, LEP2 SUSY Working Group, 2004.
- [63] DELPHI collaboration, J. Abdallah et al., *Searches for supersymmetric particles in  $e^+ e^-$  collisions up to 208-GeV and interpretation of the results within the MSSM*, *Eur. Phys. J.* **C31** (2003) 421–479, [[hep-ex/0311019](#)].
- [64] T. S. Metcalfe and P. Charbonneau, *Stellar structure modeling using a parallel genetic algorithm for objective global optimization*, *J. Comput. Phys.* **185** (2003) 176–193, [[astro-ph/0208315](#)].
- [65] MUON G-2 collaboration, G. W. Bennett et al., *Final Report of the Muon E821 Anomalous Magnetic Moment Measurement at BNL*, *Phys. Rev.* **D73** (2006) 072003, [[hep-ex/0602035](#)].
- [66] D. G. Cerdeno, M. Peiro and S. Robles, *Fits to the Fermi-LAT GeV excess with RH sneutrino dark matter: implications for direct and indirect dark matter searches and the LHC*, *Phys. Rev.* **D91** (2015) 123530, [[1501.01296](#)].
- [67] F. Calore, I. Cholis and C. Weniger, *Background Model Systematics for the Fermi GeV Excess*, *JCAP* **1503** (2015) 038, [[1409.0042](#)].
- [68] A. Achterberg, M. van Beekveld, S. Caron, G. A. Gómez-Vargas, L. Hendriks and R. Ruiz de Austri, *Implications of the Fermi-LAT Pass 8 Galactic Center excess on supersymmetric dark matter*, *JCAP* **1712** (2017) 040, [[1709.10429](#)].
- [69] FERMI-LAT collaboration, M. Ackermann et al., *The Fermi Galactic Center GeV Excess and Implications for Dark Matter*, *Astrophys. J.* **840** (2017) 43, [[1704.03910](#)].
- [70] M. Endo, K. Hamaguchi, S. Iwamoto and T. Yoshinaga, *Muon g-2 vs LHC in Supersymmetric Models*, *JHEP* **01** (2014) 123, [[1303.4256](#)].
- [71] K. Griest and D. Seckel, *Three exceptions in the calculation of relic abundances*, *Phys. Rev.* **D43** (1991) 3191–3203.
- [72] J. R. Ellis, T. Falk and K. A. Olive, *Neutralino - Stau coannihilation and the cosmological upper limit on the mass of the lightest supersymmetric particle*, *Phys. Lett.* **B444** (1998) 367–372, [[hep-ph/9810360](#)].
- [73] J. R. Ellis, T. Falk, K. A. Olive and M. Srednicki, *Calculations of neutralino-stau coannihilation channels and the cosmologically relevant region of MSSM parameter space*, *Astropart. Phys.* **13** (2000) 181–213, [[hep-ph/9905481](#)].
- [74] C. Boehm, A. Djouadi and M. Drees, *Light scalar top quarks and supersymmetric dark matter*, *Phys. Rev.* **D62** (2000) 035012, [[hep-ph/9911496](#)].
- [75] R. L. Arnowitt, B. Dutta and Y. Santoso, *Coannihilation effects in supergravity and D-brane models*, *Nucl. Phys.* **B606** (2001) 59–83, [[hep-ph/0102181](#)].
- [76] J. R. Ellis, K. A. Olive and Y. Santoso, *Calculations of neutralino stop coannihilation in the CMSSM*, *Astropart. Phys.* **18** (2003) 395–432, [[hep-ph/0112113](#)].
- [77] S. Mizuta and M. Yamaguchi, *Coannihilation effects and relic abundance of Higgsino dominant LSP(s)*, *Phys. Lett.* **B298** (1993) 120–126, [[hep-ph/9208251](#)].
- [78] J. Edsjo and P. Gondolo, *Neutralino relic density including coannihilations*, *Phys. Rev.* **D56** (1997) 1879–1894, [[hep-ph/9704361](#)].
- [79] H. Baer, C. Balazs and A. Belyaev, *Neutralino relic density in minimal supergravity with coannihilations*, *JHEP* **03** (2002) 042, [[hep-ph/0202076](#)].
- [80] A. Birkedal-Hansen and E.-h. Jeong, *Gaugino and Higgsino coannihilations. 1. Neutralino neutralino interactions*, *JHEP* **02** (2003) 047, [[hep-ph/0210041](#)].
- [81] H. Baer, T. Krupovnickas, A. Mustafayev, E.-K. Park, S. Profumo and X. Tata, *Exploring the BWCA (bino-wino co-annihilation) scenario for neutralino dark matter*, *JHEP* **12** (2005) 011, [[hep-ph/0511034](#)].

- [82] K. A. Olive and M. Srednicki, *New Limits on Parameters of the Supersymmetric Standard Model from Cosmology*, *Phys. Lett.* **B230** (1989) 78–82.
- [83] K. A. Olive and M. Srednicki, *Cosmological limits on massive LSP 's*, *Nucl. Phys.* **B355** (1991) 208–230.
- [84] J. Hisano, S. Matsumoto, M. Nagai, O. Saito and M. Senami, *Non-perturbative effect on thermal relic abundance of dark matter*, *Phys. Lett.* **B646** (2007) 34–38, [[hep-ph/0610249](#)].
- [85] D. G. Cerdeno and C. Munoz, *Neutralino dark matter in supergravity theories with non-universal scalar and gaugino masses*, *JHEP* **10** (2004) 015, [[hep-ph/0405057](#)].
- [86] M. E. Cabrera, J. A. Casas, A. Delgado, S. Robles and R. Ruiz de Austri, *Naturalness of MSSM dark matter*, *JHEP* **08** (2016) 058, [[1604.02102](#)].
- [87] GAMBIT collaboration, G. D. Martinez, J. McKay, B. Farmer, P. Scott, E. Roebber, A. Putze et al., *Comparison of statistical sampling methods with ScannerBit, the GAMBIT scanning module*, *Eur. Phys. J.* **C77** (2017) 761, [[1705.07959](#)].
- [88] CHERENKOV TELESCOPE ARRAY CONSORTIUM collaboration, B. S. Acharya et al., *Science with the Cherenkov Telescope Array*, **1709.07997**.
- [89] XENON collaboration, E. Aprile et al., *First Dark Matter Search Results from the XENON1T Experiment*, *Phys. Rev. Lett.* **119** (2017) 181301, [[1705.06655](#)].
- [90] LUX collaboration, D. S. Akerib et al., *Limits on spin-dependent WIMP-nucleon cross section obtained from the complete LUX exposure*, *Phys. Rev. Lett.* **118** (2017) 251302, [[1705.03380](#)].
- [91] LUX-ZEPLIN collaboration, D. S. Akerib et al., *Projected WIMP sensitivity of the LUX-ZEPLIN (LZ) dark matter experiment*, **1802.06039**.
- [92] DARWIN collaboration, J. Aalbers et al., *DARWIN: towards the ultimate dark matter detector*, *JCAP* **1611** (2016) 017, [[1606.07001](#)].
- [93] F. Ruppin, J. Billard, E. Figueroa-Feliciano and L. Strigari, *Complementarity of dark matter detectors in light of the neutrino background*, *Phys. Rev.* **D90** (2014) 083510, [[1408.3581](#)].
- [94] FERMI-LAT collaboration, M. Ackermann et al., *Searching for Dark Matter Annihilation from Milky Way Dwarf Spheroidal Galaxies with Six Years of Fermi Large Area Telescope Data*, *Phys. Rev. Lett.* **115** (2015) 231301, [[1503.02641](#)].
- [95] H. Baer, V. Barger and A. Mustafayev, *Implications of a 125 GeV Higgs scalar for LHC SUSY and neutralino dark matter searches*, *Phys. Rev.* **D85** (2012) 075010, [[1112.3017](#)].
- [96] L. J. Hall, D. Pinner and J. T. Ruderman, *A Natural SUSY Higgs Near 126 GeV*, *JHEP* **04** (2012) 131, [[1112.2703](#)].
- [97] A. Arbey, M. Battaglia, A. Djouadi, F. Mahmoudi and J. Quevillon, *Implications of a 125 GeV Higgs for supersymmetric models*, *Phys. Lett.* **B708** (2012) 162–169, [[1112.3028](#)].
- [98] S. Akula, B. Altunkaynak, D. Feldman, P. Nath and G. Peim, *Higgs Boson Mass Predictions in SUGRA Unification, Recent LHC-7 Results, and Dark Matter*, *Phys. Rev.* **D85** (2012) 075001, [[1112.3645](#)].
- [99] J. A. Casas, J. M. Moreno, S. Robles, K. Rolbiecki and B. Zaldivar, *What is a Natural SUSY scenario?*, *JHEP* **06** (2015) 070, [[1407.6966](#)].